Tidal disruption and ignition of white dwarfs by moderately massive black holes

S. Rosswog[1], E. Ramirez-Ruiz[2] and W.R.Hix[3]

[1] School of Engineering and Science, Jacobs University Bremen, Campus Ring 1, 28759 Bremen, Germany

[2] Department of Astronomy and Astrophysics, University of California, Santa Cruz, CA 95064

[3]Physics Division, Oak Ridge National Laboratory, Oak Ridge, TN37831-6374

Received _____; accepted _____

ABSTRACT

We present a numerical investigation of the tidal disruption of white dwarfs by moderately massive black holes, with particular reference to the centers of dwarf galaxies and globular clusters. Special attention is given to the fate of white dwarfs of all masses that approach the black hole close enough to be disrupted and severely compressed to such extent that explosive nuclear burning can be triggered. Consistent modeling of the gas dynamics together with the nuclear reactions allows for a realistic determination of the explosive energy release. In the most favorable cases, the nuclear energy release may be comparable to that of typical type Ia supernovae. Although the explosion will increase the mass fraction escaping on hyperbolic orbits, a good fraction of the debris remains to be swallowed by the hole, causing a bright soft X-ray flare lasting for about a year. Such transient signatures, if detected, would be a compelling testimony for the presence of a moderately mass black hole (below $10^5 M_\odot$).

1. Introduction

White dwarfs, the end point of stellar evolution for stars with masses from about 0.07 to 10 solar masses, are extremely common (52). And we don't have to look far away, either. There are several billions of them in the halo of our very own Milky Way galaxy (39). They are not only observed in isolation but in binary systems, with normal stellar companions, and, less frequently, with compact stellar companions. At a distance of tens of kiloparsecs, a number of globular clusters (8; 31) have a high enough central density to let white dwarfs interact and collide with other stars, or, if developed, with a central massive black hole (17; 18; 15; 16). And at a distance of less than ten kiloparsecs, our galactic nucleus, a

central massive black hole of a few million solar masses (19), is surrounded by swarms of all kind of stars, some of them white dwarfs and all of them prone to collisions. In such dense environments, stars of all varieties can exchange mass, disrupt each other or merge, and their merger products can get involved in similar interactions. Because of this reason, the innermost ~ 0.1 pc of our Galaxy can be considered an efficient stellar collider (1). Stellar dynamics is perfectly adequate in modeling the motions of stars as point masses moving under the influence of gravity, even in dense stellar systems, unless individual stars closely approach each other or get so close to the central black hole that they become vulnerable to tidal distortions. Once this happens, the internal structure of the stars becomes important for the further dynamical evolution. This paper explores the observational manifestations of such phenomena, with particular reference to white dwarfs.

A white dwarf interacting with a neutron star or a black hole cannot be treated as a point mass if it gets so close to the compact remnant that it becomes tidally deformed. The tidal interaction between a star and a black hole is mainly characterized by three length scales: the stellar radius, $R_{\rm wd}$, the gravitational radius of the black hole, $R_{\rm g} = 2GM_{\rm BH}/c^2 \simeq 3 \times 10^{11} M_{\rm BH,6}$ cm, where $M_{\rm BH,6}$ denotes the hole's mass in units of $10^6 M_\odot$, and the tidal radius, R_τ. The tidal radius, defined as the distance within which a stars gets disrupted, obviously depends on the type of star being considered. For a white dwarf it is roughly given by

$$R_\tau \simeq 1.2 \times 10^{11} M_{\rm BH,6}^{1/3} \left(\frac{R_{\rm wd}}{10^9 {\rm cm}}\right) \left(\frac{M_{\rm wd}}{0.6 M_\odot}\right)^{-1/3} {\rm cm}. \quad (1)$$

Essentially, R_τ is the distance from the hole at which $M_{\rm BH}/R_\tau^3$ equals the mean density of the passing star. R_τ is, in order of magnitude, the same as the Roche radius, which is a precisely defined quantity, but only strictly applicable to a star in a circular orbit with synchronized spin. The strength of the tidal encounter is measured by the dimensionless

parameter

$$\eta = \left(\frac{M_{\rm wd}}{M_{\rm BH}} \frac{{R_{\rm p}}^3}{{R_{\rm wd}}^3} \right)^{1/2}, \tag{2}$$

which is simply the square root of the ratio of the surface gravity of the star to the tidal gravity at the surface when the star is at pericenter distance R_p. Most literature on tidal disruption uses $\beta = R_\tau / R_p = \eta^{-2/3}$ to measure the encounter strength. When $\eta \leq 1$, the star is disrupted in a single flyby. The energy required to tear the star apart (that is, the star's self-binding energy) is supplied at the expense of the orbital energy, which at R_τ is larger by $(M_{\rm BH}/M_{\rm wd})^{2/3}$.

For white dwarfs, the ratio between the tidal disruption radius and the gravitational radius is

$$\beta_{\rm g} = \left(\frac{R_\tau}{R_{\rm g}} \right) \simeq 0.4 M_{\rm BH,6}^{-2/3} \left(\frac{R_{\rm wd}}{10^9 {\rm cm}} \right) \left(\frac{M_{\rm wd}}{0.6 M_\odot} \right)^{-1/3}. \tag{3}$$

Note that this is indeed inside the gravitational radius for black hole masses exceeding

$$M_{\rm BH,lim} \simeq 2.5 \times 10^5 \left(\frac{R_{\rm wd}}{10^9 {\rm cm}} \right)^{3/2} \left(\frac{M_{\rm wd}}{0.6 M_\odot} \right)^{-1/2} M_\odot. \tag{4}$$

For this reason, white dwarfs only experience disruptive physical conditions when approaching a moderately massive black hole (29). If $M_{\rm BH} \ll M_{\rm BH,lim}$ it is however, sufficiently far outside $R_{\rm g}$ that the disruption can be approximated as a Newtonian process, and it makes little difference whether the hole is described by a Schwarzschild or a Kerr metric. When the central hole has a mass $M_{\rm BH} \gg M_{\rm wd}$, the size of the star remains smaller than R_τ. A white dwarf cannot thus be disrupted (Figure 1) without entering the strong relativistic domain if

$$\beta > \min \left[\left(\frac{M_{\rm BH}}{M_{\rm wd}} \right)^{1/3}, \left(\frac{M_{\rm BH,lim}}{M_{\rm BH}} \right)^{2/3} \right]. \tag{5}$$

The type of the black hole (Schwarzchild or Kerr?) then has an important quantitative effect, as does (for a Kerr hole) the orientation of the stellar orbit relative to the spin axis.

Much of our effort in this paper is therefore dedicated to investigate the disruption of white dwarfs by moderately massive black holes, with particular reference to the centers

of dwarf galaxies (e.g. 30), globular clusters (e.g. 36; 3) and the intermediate-mass black hole candidates in active galactic nuclei (20). Special attention is given to the fate of white dwarfs of all masses that approach a black hole close enough to be disrupted and severely compressed to such extent that explosive nuclear burning can be triggered. Tidal disruption of white dwarfs has previously been difficult to model due to its three-dimensional nature and the delicate interplay between gravity, gas dynamics and nuclear reactions. Crucial aspects of the physics of white dwarf disruption and ignition were first understood by Luminet & Pichon (29), mainly based on the affine model earlier introduced by Carter & Luminet (9). Luminet & Pichon (29) suggested that for very close encounters ($\eta \leq 1$), relativistic effects and compression into the orbital plane could trigger significant nuclear energy release in the core (some authors, particularly Wilson & Mathews 2004 and Dearborn et al. 2005, believe such considerations could also apply to weakly disrupted encounters for which general relativistic effects can overwhelm the stabilizing tidal forces and still cause relativistic compression). The affine model of Carter and Luminet approximates the white dwarf as a time-dependent ellipsoid, with a fixed density profile. Such a model is of limited utility if the true matter distribution deviates from the assumed shape and density profile. To study the tidal disruption problem, we use a three dimensional smoothed particle hydrodynamics method (SPH) to solve the equations of hydrodynamics. This method makes no restrictive assumptions on the hydrodynamic degrees of freedom and allows us to study the three-dimensional encounter with full generality. Due to its Lagrangian nature SPH is perfectly suited to follow tidal disruption processes during which the corresponding geometry, densities and time scales are changing violently (45; 46). What is more, our consistent modeling of gas dynamics together with nuclear energy generation allows for a realistic determination of the explosive energy release.

In this paper, a comprehensive approach is adopted: we follow the tidal disruption and compression leading up to the ignition of the white dwarf (when triggered); the

accompanying nucleosynthesis and expansion of the debris; and the subsequent accretion of the bound debris. Some of the questions at the forefront of attention include the effects of initial composition and mass of the white dwarf, the passage distance, and the black hole's mass on ignition and disruption, and the degree to which the post-disruption dynamics is modified by nuclear energy release. We address all of these issues here.

A detailed description of the numerical methods and the initial models is given in §2. Detailed hydrodynamic simulations of the disruption of white dwarfs of various masses, initial composition and passage distances are presented in §§3, 4 and 5, the role of the mass of the black hole in shaping the evolution and ignition of the disrupted white dwarf is discussed in §4. The resulting gravitational wave signals are shown in §6. Discussion and conclusions are presented in §7.

2. Numerical Methods and Initial Model

The observational consequences of stellar disruption depend on what happens to the debris (40; 13; 27). To quantify this, we have performed detailed three-dimensional, hydrodynamical calculations. The gas dynamics is coupled with a nuclear network to explore the effects of nuclear energy generation during the strong compression phase. The reader is referred to Rosswog et al. (45) for a complementary description of the numerical methods employed in calculating the disruptive event.

2.1. Hydrodynamics

The SPH-formulation used in this study follows closely the one described in Benz (5), a brief derivation of the equations can be found in Rosswog & Price (47). Forces from self-gravity are calculated using a binary tree (6) while the gravitational forces from the

central black hole are calculated using a Paczyński-Wiita pseudo potential (34) with a polynomial extension (43) to avoid the singularity at the Schwarzschild radius. We have taken particular care to avoid artifacts from the use of artificial viscosity (AV). The so-called Balsara-switch (2) is implemented to avoid spurious shear forces. More importantly, we use time dependent viscosity parameters (32), so that far from shocks artificial viscosity is essentially absent, but near a shock front the associated viscous parameters rise to values that are able to avoid post-shock oscillations (see Fig. 1 of (45) for an illustration). Once the shocks has passed, the parameters decay again. Details of the AV implementation and tests can be found in (41).

A MacCormack predictor-corrector method is used to evolve the fluid in time. The method is implemented with individual time steps, i.e. each particle i is advanced on its own time step $dt_i = 2^{n_i} \times dt_{\rm min}$, where $dt_{\rm min}$ is the smallest step of all the particles. n_i is chosen to be the largest integer satisfying the condition $dt_i < dt_{i,\rm des}$, where $dt_{i,\rm des}$ is the desired time step for particle i. With this time marching implementation the total energy is conserved to better than 4×10^{-3} and the total angular momentum to better than 2×10^{-4}. Note that this could, in principle, be improved even further by taking into account the so-called "grad-h"-terms (49; 33) and extra-terms arising from adapting gravitational smoothing terms (37). A comparison between the formulation used here and the one using "grad-h"-terms can be found in Rosswog & Price (44).

2.2. Equation of State

We use the HELMHOLTZ equation of state (EOS), developed by the Center for Astrophysical Thermonuclear Flashes at the University of Chicago. The EOS allows to freely specify the chemical composition of the gas and it can be coupled to a nuclear reaction network. The electron-/positron equation of state is calculated without approximation.

In other words, it makes no assumption about the degree of degeneracy or relativity and the exact expressions are integrated numerically. The nuclei in the gas are treated as a Maxwell-Boltzmann gas, the photons as blackbody radiation. The EOS is used in tabular form with densities in the range $10^{-10} \leq \rho Y_e \leq 10^{11}$ g cm^{-3} and temperatures varying between 10^4 and 10^{11} K. A sophisticated, biquintic Hermite polynomial interpolation is used to enforce the thermodynamic consistency (i.e. the Maxwell-relations) at interpolated values (51).

2.3. Nuclear Burning

To account for the feedback onto the fluid from nuclear transmutations we use a minimal nuclear reaction network developed by Hix et al. (23). It couples a conventional α-network stretching from He to Si with a quasi-equilibrium-reduced α-network. The QSE-reduced network neglects reactions within small equilibrium groups that form at temperatures above 3.5×10^9 K to reduce the number of abundance variables needed. Although a set of only seven nuclear species is used, this network reproduces all burning stages from He-burning to NSE accurately. For details and tests we refer to Hix et al. (23).

The network is coupled to the hydrodynamics in an operator splitting fashion, i.e. hydrodynamics and nuclear burning -which may in extreme cases require vastly different time steps- are integrated separately. In a first step, the hydrodynamic equations are integrated with the above described predictor-corrector scheme to obtain new quantities at time step t^{n+1}. In this step we ignore the nuclear source term in the energy equation, the new value for the specific energy of particle a is denoted by $\tilde{u}_a^{n+1}$. The specific energy has

to be corrected for the energy release that occurred between t^n and t^{n+1}:

$$\epsilon_{a,n\rightarrow n+1} = -N_{\rm A}\sum_j m_j c^2 \int_{t^n}^{t^{n+1}} \frac{dY_{j,a}}{dt}(\rho_a(t), T_a(t), Y_{k,a}(t))\, dt \quad (6)$$

$$= -N_A \sum_{j=1} m_j c^2 (Y_{j,a}^{n+1} - Y_{j,a}^n), \quad (7)$$

where $N_{\rm A}$ is Avogadro's constant, $m_j c^2$ is the mass energy of nucleus j and $Y_{j,a}$ is the abundance of nucleus j in particle a. We use $\rho_a(t) \approx \rho_a(t^n) + \frac{t-t^n}{t^{n+1}-t^n}\{\rho_a(t^{n+1}) - \rho_a(t^n)\}$ and $T_a(t) \approx \frac{t-t^n}{t^{n+1}-t^n}\{\tilde{T}_a(t^{n+1}) - T_a(t^n)\}$, where $\tilde{T}_a(t^{n+1})$ is the temperature derived from $\tilde{u}_a^{n+1}$, to integrate the abundances $Y_{j,a}$ via the implicit backward Euler method (the network integration is described in detail in (23))[1]. The final value for the specific energy at time t^{n+1} is given by

$$u_a^{n+1} = \tilde{u}_a^{n+1} + \epsilon_{a,n\rightarrow n+1}. \quad (8)$$

The EOS is then called again to make all thermodynamic quantities consistent with this new value u_a^{n+1}. Once the derivatives have been updated, the procedure can be repeated for the next time step. For details of the time step criteria we refer the reader to Rosswog et al. (45).

As will be shown below, the peak compression occurs at a spatially fixed point (see density panels in Fig. 6). The white dwarf fuel is fed with free-fall velocity $v_{\rm ff} = (2GM_{\rm BH}/R_{\rm p})^{1/2} = 1.6 \cdot 10^5 \ {\rm km\ s^{-1}}\ \ (M_{\rm BH}/1000\ {\rm M_\odot})^{1/2}\,(R_{\rm p}/10^4\ {\rm km})^{-1/2}$ into this compression point. This is many orders of magnitude larger than typical flame propagation speeds, therefore flame propagation effects can be safely neglected for this investigation.

[1]Note that the temperature evolution along a hydrodynamical time step is different from the description in Rosswog et al. (45). In practice, we only see tiny differences between both approaches.

2.4. Initial Model

It is a vital ingredient for any calculation to start out from initial conditions that are as accurate as possible. In order to build stars in hydrostatic equilibrium, it is therefore necessary to find SPH particle distributions whose number density reflects the equilibrium mass density distribution. To this end we solve the spherically symmetric Lane-Emden equations for a star of given mass and composition to find a one dimensional density profile. For simplicity, and to start from a conservatively low value, we assume a uniform temperature of $T_0 = 5 \times 10^4$ K. This assumption will be relaxed in one run (run 10, see Table 1) to test for the sensitivity to this initial condition. Once the solution to the Lane-Emden equation has been obtained, we distribute the desired number of particles, N, inside a unit sphere according to a close-packed configuration. Subsequently, we map this distribution into the volume of the star that is to be constructed. As an example, the particle distributions before and after mapping of a 0.2 $M_\odot$ white dwarf are shown in Figure 2.

The mapping of the initial configuration is done so that the SPH-particle number density in the star, n, yields

$$\rho_{\rm LE}(r) = m \cdot n(r), \tag{9}$$

where m is the mass of each particle and $\rho_{\rm LE}$ is the density profile obtained by solving the Lane-Emden equation. We denote quantities referring to the star (unit sphere) with (un-)primed variables. If the unit sphere has a constant density ρ_0 and contains N particles, each with mass $m = M_{\rm wd}/N$, the mass in the shell between r_{n-1} and r_n is $M_n \simeq 4\pi r_{n-1}^2 \Delta r \rho_0$. As illustrated in Figure 3, the image of this shell (in the star) contains the same mass, but now between r'_{n-1} and r'_n, so that $M'_n \simeq 4\pi r'^2_{n-1} \Delta r'_n \rho_{n-1}$. The condition $M'_n = M_n$ then yields

$$\Delta r'_n = \left(\frac{r_{n-1}}{r'_{n-1}}\right)^2 \left(\frac{\rho_0}{\rho'_{n-1}}\right) \Delta r. \tag{10}$$

The resultant configuration is very close to hydrostatic equilibrium. To find the "real" numerical equilibrium state we relax this configuration with the full hydrodynamics code by applying an artificial, velocity dependent damping force as, for example, in Rosswog et al. (42).

We use this procedure for all but the heaviest white dwarfs (1.2 $M_\odot$). Since their adiabatic exponent is already approaching the critical 4/3, these stars are very centrally condensed and, as a result, the bulk of the SPH particles resides very close to each other in the stellar center. This would, even for a moderate resolution of a few hundred thousand particles, result in most of the particles running at time steps that are orders of magnitude smaller than the dynamical time of the star. To alleviate this computational burden in the heaviest white dwarfs we allow for slightly different particle masses (about a factor of 10 from the center to the stellar surface).

Throughout this simulation set we assume a uniform nuclear composition accross the white dwarfs. Stars with masses < 0.6 $M_\odot$ are instantiated as pure helium, more massive stars are modeled as 50% carbon and 50% oxygen. Note that helium core burning may produce composition gradients throughout the stars with oxygen being more abundant in the stellar core. Since it is mainly the core that becomes ignited during the compression, see Sect. 3, such a gradient may slightly reduce the nuclear energy that can be released in principle.

Common to all calculations is the initiation of the calculations with the white dwarf being placed safely outside R_τ. Initial separations are at least twice, in most cases three times the tidal radius to allow the initially spherical star to adjust properly to the changing tidal potential as it approaches the black hole. All stars are set onto parabolic orbits so that R_p is larger than R_g.

The performed runs are summarized in Table 1.

3. Events in the Life of a Tidally Disrupted White Dwarf

Since the focus of this study is closely related to the nuclear energy release during strong encounters, practically all following calculations refer to cases with penetration factors β clearly beyond unity, see Table 1. To illustrate the evolution of a white dwarf that is just marginally disrupted, we show in Fig. 4 a 0.6 $M_\odot$ CO white dwarf that passes a 1000 $M_\odot$ black hole with a penetration factor of $\beta = 0.9$ (run 10, Table 1; keep in mind that the tidal radius as defined above is approximate and its exact value depends in the internal structure of the disrupted star). The upper panel shows snapshots at t=0.34, 3.43, 6.86, 10.29, 13.72, 17.15, 20.58 and 24.01 s after the simulation start at a separation of 3 R_τ. The lower panel shows late stages at t= 138.24 and 380.53 s. The circle indicates in both cases the location of the tidal radius. At about 1.5 R_τ the star becomes noticeably deformed and substantially spun up by the time it reaches pericentre (snapshot 5, upper panel). While receeding from the black hole large, puffed-up lobes form at the extremes of the star. The inner lobe returns to the black hole (see t=138.24 s, lower panel) while the outer is ejected to infinity, both are connected by a well-defined and homogenous spaghetti-like tube of white dwarf debris.

The opposite limit, an exremely strong encounter, is illustrated in Figure 5. The snapshots are taken from our numerical simulations of a 0.2 $M_\odot$ white dwarf approaching a $10^3 M_\odot$ black hole on a parabolic orbit with pericenter distance well within the tidal radius ($R_\mathrm{p} = R_\tau/12$; run 1 in Table 1). While falling inwards towards the hole, the white dwarf develops a quadrupole distortion, which attains an amplitude of order unity by the time of disruption at $R \sim R_\tau$.

When the star is still far from the black hole, it remains close to its initial stationary equilibrium state as characterized by the usual virial relation. This is because the timescale characterizing the rate of change of the tidal force will initially be very long compared with

the intrinsic timescale characterizing the corresponding quadrupole oscillations of the star. The tidal bulge raised on the star by the black hole becomes an order unity distortion near the tidal radius. The resultant gravitational torque spins it up to a good fraction of its corotation angular velocity by the time it gets disrupted. The large surface velocities and the order unity tidal bulge combine to overcome the star's self gravity and lead to the disruption of the star.

Our present investigation is concerned with cases of deeper penetration within the tidal radius so that the core as well as the envelope are affected. The behavior of a white dwarf passing well within the tidal radius exhibits special features (9; 7). As illustrated in Figure 6, the degenerate star is not only elongated along the orbital direction but also severely compressed perpendicular to the orbital plane. This anisotropy can be understood as arising from the fact that the principal tidal axes within the orbital plane will rotate prior to pericenter passage so that the corresponding effects of elongation and compression will roughly cancel out, whereas the third principal axis retains a fixed direction so that compression orthogonal to the orbital plane is uncontested (see, e.g., the appendix of (4)). Each section of the star is squeezed through a point of maximum compression at a fixed point on the star's orbit. This takes place on a timescale comparable to the crossing time of the star through periastron,

$$\delta t \sim \frac{R_{\rm wd}}{v_{\rm p}} \simeq 0.2 \left(\frac{M_{\rm wd}}{0.6 M_\odot}\right)^{-1/6} \left(\frac{R_{\rm wd}}{10^9 {\rm cm}}\right)^{3/2} \left(\frac{M_{\rm BH}}{10^3\ M_\odot}\right)^{-1/3} \ {\rm s}, \tag{11}$$

where

$$v_{\rm p} \sim (R_{\rm g}/R_\tau)^{1/2} c \simeq 5 \times 10^9 \left(\frac{M_{\rm wd}}{0.6 M_\odot}\right)^{1/6} \left(\frac{R_{\rm wd}}{10^9 {\rm cm}}\right)^{-1/2} \left(\frac{M_{\rm BH}}{10^3\ M_\odot}\right)^{1/3} \ {\rm cm\ s^{-1}}, \tag{12}$$

is the orbital velocity at periastron.

During this very short lived phase, the star attains its maximum degree of compression (here by a factor ~ 100) although its orbital-plane section increases only by a factor of a

few due to the continually changing directions of the two principal tidal axis (Figure 6). The distortions $\Delta R_{\rm wd}/R_{\rm wd} \sim 1$ impart supersonic bulk flow velocities of order

$$\frac{R_{\rm wd}}{\delta t} \sim v_{\rm p} \ll c_s \sim 2.8 \times 10^8 \left(\frac{R_{\rm wd}}{10^9{\rm cm}}\right)^{-1/2} \left(\frac{M_{\rm wd}}{0.6\ M_\odot}\right)^{1/2}\ {\rm cm\ s^{-1}} \tag{13}$$

during the drastic compression of the stellar material. This compression is thus halted by a shock (27; 4), raising the matter, which then rebounds perpendicular to the orbital plane, to a higher adiabat (Figure 7). As a result, the temperatures increase sharply and trigger explosive burning (of He for the case shown in Figure 6).

The typical temperature of the shocked star and the thermal energy produced by shock heating can be roughly estimated from the virial theorem as

$$T \sim 6 \times 10^8 \left(\frac{R_{\rm wd}}{10^9{\rm cm}}\right)^{-1} \left(\frac{M_{\rm wd}}{0.6\ M_\odot}\right)\ {\rm K}, \tag{14}$$

and

$$E_{\rm therm} \sim E_{\rm G} \sim 10^{50} \left(\frac{R_{\rm wd}}{10^9{\rm cm}}\right)^{-1} \left(\frac{M_{\rm wd}}{0.6\ M_\odot}\right)^{2}\ {\rm erg}. \tag{15}$$

Adiabatic compression alone can only increase the stellar surface and interior layer temperatures by a modest factor. If adiabatic compression was the only source of heating, the response to the flow to the varying potential would be $\sim R_{\rm wd}/c_s \sim 4$ s, which is significantly longer than the dynamic crossing time.

The evolution of the abundances (for the simulation shown in Figure 5) is shown in Figure 8, within the 12 s during which the entropy increases the fastest. During the about one second long period of compression, the temperature increases beyond 3×10^9K, approaching but not quite reaching nuclear statistical equilibrium (NSE). During this brief period of compression, nuclei up to and beyond Si are synthesized. The initial composition was pure He and the final mass fraction in iron-group nuclei is about 15%. This result should be taken as a modest underestimate, since the seven species nuclear network only provides an approximation to the detailed nuclear processes. Post-processing calculations,

using a 300 isotope nuclear network over thermodynamic particle histories resulting from these calculations, show significant nuclear flow above silicon, for helium-rich portions of the gas with peak temperatures above 2×10^9K. As a result, heavier elements (like calcium, titanium and chromium) would be made, accompanied by a modest increase in the energy generation. It is thus safe to conclude that the white dwarf is tidally ignited and that a sizable mass of iron-group nuclei is injected into the outflow.

The variation of the specific energy in the released gas, in the absence of explosive energy input, is determined mainly by the relative depth of a mass element across the disrupted star in the potential well of the black hole (40). This is much larger than the binding energy and the kinetic energy generated by spin-up near pericenter. Even though the mean specific binding energy of the debris to the hole is comparable with the self-binding energy of the original star, the spread about this mean is larger by a factor $(M_{\rm BH}/M_{\rm wd})^{1/3}$. Nuclear energy released during the drastic compression and distortion of the stellar material, further enhances the spread in specific energies at pericenter (Figure 9), and, as a result, the mass fraction escaping on hyperbolic orbits is increased from $\sim 50\%$ to $\sim 65\%$ of the initial mass of the white dwarf. The mass fraction that is ejected rather than swallowed, though less spectacular than typical Type Ia supernovae (22), should have many distinctive observational signatures (the reader is referred to Kasen et al. 2008 for a detailed description of the optical light curves and spectra resulting from the unbound debris before it becomes translucent). First, the explosion itself should be different, since the disrupted, degenerate stars should be, on average, lighter than those exploding as type Ia supernovae. Second, the spectra should exhibit large Doppler shifts, as the ejected debris would be expelled with speeds $\geq 10^4$ km/s. Finally , the optical light curve should be rather unique as a result of the radiating material being highly squeezed into the orbital plane (one thus expects different timescales for conversion of nuclear energy to observable luminosity when compared with normal type Ia events).

Although the explosion will increase the fraction of ejected debris, a good fraction ($\sim 35\%$) remains to be accreted on to the hole. The returning gas does not immediately produce a flare of activity from the black hole. First material must enter quasi circular orbits and form an accretion torus (40; 13). Only then will viscous effects release enough binding energy to power a flare. The bound orbits are very eccentric, and the range of orbital periods is large. For white dwarfs, the orbital semi-major axis of the most tightly bound debris is

$$a \sim 300 \left(\frac{M_{\rm BH}}{10^3\ M_\odot}\right)^{-1/3} \left(\frac{R_{\rm wd}}{10^9{\rm cm}}\right) \left(\frac{M_{\rm wd}}{0.6\ M_\odot}\right)^{-2/3}\ R_{\rm g}, \tag{16}$$

and the period is only

$$t_{\rm a} \sim 150 \left(\frac{a}{300 R_{\rm g}}\right)^{3/2} \left(\frac{M_{\rm BH}}{10^3\ M_\odot}\right)^{-1/2}\ {\rm s}. \tag{17}$$

If the gaseous debris suffered no internal dissipation due to high viscosity or shocks, it would, after one or two orbital periods, form a highly elliptical disc with a big spread in apocenter distances between the most and least bound orbits, but where at pericenter, $R_{\rm p}$, the radial focusing of the orbits acts as an effective nozzle (Figure 4 and 10). After pericenter passage, the outflowing gas is on orbits which collide with the infalling stream near the original orbital plane at apocenter, giving rise to an angular momentum redistributing shock (Figure 10) much like those in cataclysmic variable systems. The debris raining down would, after little more than its free-fall time, settle into a disc. This orbiting debris starts to form when the most tightly bound debris falls back. The simulation shows that the first material returns at a time $\leq t_{\rm a}$, with an infall rate of about $10^2 M_\odot\ {\rm yr}^{-1}$ (Figure 11). Such high infall rates are expected to persist, relative steadily, for at least a few orbital periods, before all the highly bound material rains down. The vicinity of the hole would thereafter be fed solely by injection of the infalling matter. The early mass infall rate is sensitive to the stellar structure (28; 38), at late times, $t \geq t_{\rm fb} \approx 600$ s, it drops off as $t^{-5/3}$ (40; 35).

Once the torus is formed, it will evolve under the influence of viscosity, radiatively cooling winds and time dependent mass inflow.

A luminosity comparable to the Eddington value, $\sim L_{\rm Edd} = 10^{41}(M_{\rm BH}/10^3 M_\odot)$ erg s^{-1}, can therefore only be maintained for at most a year; thereafter the flare would rapidly fade. It is clear that most of the debris would be fed to the hole far more rapidly than it could be accepted if the radiative efficiency were high; much of the bound debris must either escape in a radiatively-driven outflow or be swallowed inefficiently. The rise and the peak bolometric luminosity can be predicted with some confidence. However, the effective surface temperature (and thus the fraction of luminosity that emerges predominantly in the soft X-ray band) is harder to predict, as it depends on the size of the effective photosphere that shrouds the hole. Such transient signals, if detected, would be a compelling testimony for the presence of moderately massive black holes in the centers of globular clusters and dwarf galaxies.

4. Influence of Black Hole's Mass on Disruption

The characteristic tidal radius, R_τ, for a given white dwarf star is solely determined by the black hole's mass, while the strength of the tidal encounter is traditionally measured by the dimensionless parameter $\beta = R_\tau/R_{\rm p}$ (provided $\beta \leq \beta_{\rm g}$). The aim of this section is to illustrate, with the help of a few specific calculations, the role of the black hole's mass in shaping the evolution and ignition of the disrupted white dwarf. To quantify this, we have performed detailed three-dimensional, hydrodynamical calculations of the dynamics of a $0.2M_\odot$ white dwarf approaching black holes of various masses on parabolic orbits with $\beta = 5$. For black hole masses $10^2 M_\odot \leq M_{\rm BH} \leq 10^4 M_\odot$ and $\beta = 5$, a $0.2M_\odot$ white dwarf can be disrupted without entering the strong relativistic domain (Figure 1). However, complete disruption occurs sufficiently close to the hole for a Newtonian approximation to

be inadequate (Figure 12).

The behavior of a $0.2M_\odot$ white dwarf approaching black holes of various masses is illustrated in Figure 13. As discussed previously, the effects of the black hole's mass (for a fixed β and $M_{\rm wd}$) will be to move the critical pericentric distance by $M_{\rm BH}^{1/3}$ and change the star's crossing time through the maximum compression point by $M_{\rm BH}^{-1/3}$. As a result, stars approaching black holes of increasing mass will appear more elongated along the orbital plane, as each section of the star is squeezed faster through a point of maximum compression at a fixed point on the star's increasingly extended orbit. Such stars are not only more elongated but are even more severely compressed into a prolate shape. If the initial white dwarf is made of pure He (as in the 0.2 $M_\odot$ case), the combustion rate will be determined by the 3α reaction, on time scale approximately given by (26)

$$t_{\rm b} \approx 9.0 \times 10^{-4} T_9^3 \exp(4.4/T_9)\ \rho_6^{-2}, \tag{18}$$

where T_9 is the temperature in units 10^9 K and ρ_6 the density in 10^6 gcm^{-3} .

If the time scale on which the white dwarf can react, its dynamical time scale $t_{\rm G} = (G\bar{\rho}_{\rm wd})^{-1/2}$, is much shorter than the burning time scale $t_{\rm b}$, the star can expand rapidly enough to quench burning by a reduction of temperature and density. Appreciable burning will therefore only take place if $t_{\rm b} \ll t_{\rm G}$. As illustrated in Figure 14, this comparison of time scales can be used as a simple estimate for whether or not substantial He-burning will occur. Promising models for thermonuclear explosions are those that reach high temperatures at high densities (upper right corner). For a fixed β, increasing $M_{\rm BH}$ raises the nuclear energy release. For black hole masses $M_{\rm BH} > 10^2$ M$_\odot$, nuclear energy released during the drastic compression and distortion of a 0.2 $M_\odot$ white dwarf approaching moderately massive black holes with $\beta = 5$ is fast enough to release energy in excess of that required to tear the star apart: $E_{\rm G}$ (Figure 15). When the black hole mass is $\gg 10^4 M_\odot$ most white dwarfs would be, however, swallowed whole ($R_\tau < R_{\rm g}$).

5. Tidal Disruption for a Variety of White Dwarfs

White dwarfs are thought to be the final evolutionary state of all stars whose mass is below ~ 10 $M_\odot$ (52). Stars with masses less than about half a solar mass become degenerate before helium ignition, and therefore will end their lifes as helium white dwarfs. In isolation, such low mass stars have life times much longer than the present age of the Universe. Still, such He white dwarfs are observed, they are thought to be the result of the evolution of a close binary system (e.g. 21). Stars of low or medium mass, achieve helium burning and become carbon-oxygen white dwarfs (perhaps the commonest sort). The observed white dwarf mass distribution is strongly peaked around 0.6 $M_\odot$ (25).
When a white dwarf is subject to strong tidal compression, triggering of nuclear processes in the stellar cores depends on initial composition. To investigate this dependence, we have performed calculations with various white dwarf masses/compositions. As outlined above, our white dwarf models are initialized with pure He-composition for $M_{\rm wd} < 0.6$ $M_\odot$ and 50% carbon and 50% oxygen otherwise.

Although the thermodynamical evolution and the nuclear energy release are very sensitive to the initial stellar composition (in this text, we have so far considered only a pure ^{4}He 0.2 $M_\odot$ white dwarf), we found that ignition is in fact a natural outcome for white dwarfs of all masses passing well with in the tidal radius. For example, a C/O $1.2M_\odot$ white dwarf (here assumed to be composed of 50% carbon and 50% oxygen throughout the star) approaching a 500 $M_\odot$ black hole on a parabolic orbit with pericenter distance $\beta = 3.2$ ignites (Figure 16) and, as a result, at least 0.6 $M_\odot$ of Fe are synthesised in the flow (Figure 17). Similarly, at least 0.66 $M_\odot$ of Fe are synthesised when a C/O $1.2M_\odot$ white dwarf approaches a $10^3 M_\odot$ black hole with $\beta = 3$. By contrast with the previous two cases, explosive energy release is too slow to release much energy on a dynamical timescale when a C/O $1.2M_\odot$ white dwarf approaches a $10^3 M_\odot$ black hole with $\beta = 1.5$ and, as a result,

only $1.4 \times 10^{-2} M_\odot$ of Fe are synthesised.

0.18 $M_\odot$ of Fe are synthesised when a typical 0.6 $M_\odot$ C/O white dwarf approaches a 500 $M_\odot$ black hole with $\beta = 5$. To explore how sensitive our models are to the initial temperature, we have re-run this simulation, but now with a hot white dwarf. The initial specific energy of a cold ($T = 5 \times 10^4$ K) equilibrium model was adjusted in a way that the temperature varied linearly between 5×10^7 K in the centre to 5×10^4 K at the stellar surface. In the subsequent relaxation the star expanded slightly, since the degeneracy was lifted to a small extent. As a result of the reduced degeneracy, lower peak temperatures and densities are reached (see Figure 18), reducing slightly the amount of nucleosynthesis which takes place. We consider the shown results as representative, but the actual range of behaviour for given sets of masses and orbits may be wider due to gradients in temperature and nuclear composition which have not been explored systematically here. To summarize, in the most favorable cases, the nuclear energy release, is comparable to that of typical Type Ia supernovae.

In the tidal pinching process, explosive nucleosynthesis is likely to proceed only for white dwarfs passing well within the tidal radius (Figure 19). Explosive energy release, as calculated here, appears to be a natural outcome for 0.6 $M_\odot$ (1.2 $M_\odot$) white dwarfs approaching moderately massive black holes with $\beta \geq 5$ ($\beta \geq 3$).

6. Gravitational Waves

A white dwarf approaching the tidal radius will be disrupted in a single flyby. The resulting stellar debris trail is not compact enough to emit strong gravitational waves after leaving R_p. The detectable gravitational wave signal will therefore have a burst-like

behavior, roughly characterized by an amplitude h and a duration $t \sim 1/f$, where

$$h \approx \frac{G}{c^4}\frac{\ddot{Q}}{D} \sim \frac{GM_{\rm wd}R_{\rm g}}{c^2 R_p D} \sim 7\times10^{-20}\,\beta\left(\frac{D}{10{\rm kpc}}\right)^{-1}\left(\frac{M_{\rm wd}}{0.6M_\odot}\right)^{4/3}\left(\frac{R_{\rm wd}}{10^9\ {\rm cm}}\right)^{-1} M_{\rm BH,3}^{2/3}, \quad (19)$$

and

$$f \sim \left(\frac{GM_{\rm BH}}{R_{\rm p}^3}\right)^{1/2} \sim 0.3\,\beta^{3/2}\left(\frac{M_{\rm wd}}{0.6M_\odot}\right)^{1/2}\left(\frac{R_{\rm wd}}{10^9\ {\rm cm}}\right)^{-3/2}\ {\rm Hz}. \quad (20)$$

LISA will be able to detect gravitational waves of amplitude $h \sim 10^{-21}$ for burst sources in the frequency range $f \sim 10^{-4} - 10^{-1}$Hz (11). Gravitational waves from white dwarf stellar disruption could thus be detectable if $M_{\rm wd} \geq 0.4\ M_\odot$ and the source distance $D \leq 10$ kpc (Figure 20).

The gravitational wave amplitudes h_+ and $h_\times$ shown in Figure 21 are calculated in the quadrupole approximation. The reduced quadrupole moments can be written in terms of the SPH-particle properties (10)

$$I_{jk} = \sum_i m_i(x_{ji}x_{ki} - \frac{1}{3}\delta_{jk}r_i^2). \quad (21)$$

The second time derivatives, $\ddot{I}_{jk}$, can then be expressed in terms of the particle properties by simple, direct differentiation. The retarded gravitational wave amplitudes for a distant observer along the z -axis at distance D are given by

$$D\,h_+ = \frac{G}{c^4}(\ddot{I}_{xx} - \ddot{I}_{yy}) \quad (22)$$

and

$$D\,h_\times = 2\frac{G}{c^4}\ddot{I}_{xy}. \quad (23)$$

Both duration and amplitudes of the gravitational wave bursts that are produced by the disruption calculations (Figure 21) are in agreement with the simple estimates given above.

7. Discussion

This paper presents a computational investigation of the mechanical and nuclear evolution of white dwarfs passing well within the tidal radius of a moderately massive black hole. A comprehensive top to bottom approach is adopted: we follow the tidal disruption and compression leading up to the ignition of the white dwarf; the complex propagation of the nuclear energy release through the star; the resultant gravitational wave signal and the subsequent accretion of the bound debris.

This paper has outlined several potentially observable effects. The detection of a peculiar, underluminous thermonuclear explosion (46; 24) accompanied by a thermal transient signal of predominantly soft X-rays with a peak luminosity $L \sim L_{\rm Edd} = 10^{41} M_{BH,3}$ erg/s, fading within a year would, if detected, be a compelling testimony for the existence of a new mechanism by which white dwarf ignition can be achieved. Although the thermodynamical and nuclear energy of the star is sensitive to the initial composition, we found that thermonuclear ignition is a natural outcome for white dwarfs of all masses passing well within the tidal radius, with lighter stars requiring deeper penetration into the tidal radius due to their lower densities. For simplicity, we have instantiated our initial carbon oxygen white dwarf models ($\rm M_{WD} \geq 0.6\ M_{\odot}$) as homogeneously mixed stars with a 50% mass fraction of each nucleus. While such internal chemical profiles are likely accurately realized in nature in very massive white dwarfs ($\sim 1\ \rm M_{\odot}$) (Mazzitelli & Dantona), for lower masses the gravothermal adjustment of the interior during the cooling phase produces oxygen-enhanced stellar cores surrounded by very carbon-rich mantles ($X_C \sim 0.8$). The exact radial distribution depends on the exact value of $^{12}C(\alpha,\gamma)^{16}O$ rate and the details of how convection proceeds (Mazzitelli & Dantona; 48; 50), but this general stratification tendency is well-established. Thus, the disruption of a standard 0.6 $\rm M_{\odot}$ white dwarf should produce a highly carbon-enriched remnant atmosphere. Maybe, the recently detected

carbon-rich transient SCP 06F6 accompanied by an X-ray signal (14) is already the first example for this class of object.

The gravitational forces from the central black hole are currently calculated using a Paczyński-Wiita pseudo potential but our goal is to incorporate the effects of general relativity, as white dwarfs passing well within the tidal radius cannot be disrupted without entering the strong relativistic regime. The form of the black hole (Schwarzschild or Kerr?) then has an important quantitative effect, as does (for a rotating Kerr hole) the orientation of the stellar orbit relative to the black hole spin axis. The orbits are then not ellipses, but may turn through 2π or even more (29). A fluid element, which in the case of an elliptical orbit would cross the orbital plane just once, may then have two or more traversals. This opens up the possibility of multiple shocks.

For a white dwarf which does not pass close enough to the hole to release much energy on a dynamical timescale, adiabatic cooling would severely reduce the internal radiative content before the debris became translucent (just as a supernova would be optically inconspicuous in the absence of continuing energy injection in the months after the explosion). There would be no transient until, as discussed above, the bound debris fell back onto the hole after $t_{\rm fb}$. The integrated output from this flare could, in principle, amount to a few per cent of the white dwarf's rest mass, but would probably be significantly less, because most of the debris would be fed to the black hole far more rapidly than it could be accepted if the radiative efficiency were high; much would then be swallowed inefficiently or most likely escape in radiatively-driven directed outflow: its ram pressure and subsequent heating could inhibit the steady accretion that would otherwise be inevitable in any galaxy or globular cluster harboring a moderately massive black hole.

We thank Holger Baumgardt, Peter Goldreich, Jim Gunn, Piet Hut, Dan Kasen, Bronson Messer and Martin Rees for very useful discussions. E. R. acknowledges support

from the DOE Program for Scientific Discovery through Advanced Computing (SciDAC; DE-FC02-01ER41176). The simulations presented in this paper were performed on the JUMP computer of the Höchstleistungsrechenzentrum Jülich. Oak Ridge National Laboratory is managed by UT-Battelle, LLC, for the U.S. Department of Energy under contract DE-AC05-00OR22725.

REFERENCES

Alexander, T. 2005, Phys. Rep., 419, 65

Balsara, D. S. 1995, J. Comp. Phys., 121, 357

Baumgardt, H., Makino, J., & Ebisuzaki, T. 2004, ApJ, 613, 1143

Brassart, M., & Luminet, J.-P. 2008, A&A, 481, 259

Benz, W. 1990, Numerical Modelling of Nonlinear Stellar Pulsations Problems and Prospects, 269

Benz, W., et al. 1990, ApJ, 348, 647

Bicknell, G. V., & Gingold, R. A. 1983, ApJ, 273, 749

Brodie, J. P., & Strader, J. 2006, ARA&A, 44, 193

Carter, B., & Luminet, J.-P. 1983, A&A, 121, 97

Centrella, J. M., & McMillan, S. L. W. 1993, ApJ, 416, 719

Danzmann, K. 2003, Advances in Space Research, 32, 7, 1233

Dearborn, D.S.P., Wilson, J.R. and Mathews, G.J. 2005, ApJ, 630, 309

Evans, C. R., & Kochanek, C. S. 1989, ApJ, 346, L13

Gaensicke, B.T., Levan, A.J., Marsh, T.R. & Wheatley, P.J. 2008, 2008arXiv0809.2562

Gebhardt, K., Rich, R. M., & Ho, L. C. 2002, ApJ, 578 L41

Gebhardt, K., Rich, R. M., & Ho, L. C. 2005, ApJ, 634, 1093

Gerssen, J., et al. 2002, AJ, 124, 124, 3270

Gerssen, J., et al. 2003, AJ, 125, 376

Ghez, A. M., Klein, B. L., Morris, M., & Becklin, E. E. 1998, ApJ, 509, 678

Greene, J.E & Ho, L.C 2004, ApJ, 610, 722

Heber, U., Science 2002, 296, 2344

Hillebrandt, W., & Niemeyer, J. C. 2000, ARA&A, 38, 191

Hix, W. R., et al. 1998, ApJ, 503, 332

Kasen , D., Ramirez-Ruiz, E. & Rosswog, S. 2008, submitted to ApJ

Kepler, S.O. et al., MNRAS 2006, 375, 1315

Khokhlov, A. M. & Ergma, E. V. 1986, Soviet Astronomy Letters 12, 152

Kobayashi, S., Laguna, P., Phinney, E. S., & Mészáros, P. 2004, ApJ, 615, 855

Lodato, G., King, A.R. & Pringle, J.E. 2008, arXiv:0810.1288

Luminet, J.-P., & Pichon, B. 1989, A&A, 209, 103

Mathur, S., Ghosh, H., Ferrarese, L., & Fiore, F. 2008, arXiv:0807.0422

Mazzitelli, I. & Dantona, F., ApJ 1986, 311 762

Moehler, S., & Bono, G. 2008, arXiv:0806.4456

Morris, J., & Monaghan, J. 1997, J. Comp. Phys., 136, 41

Monaghan, J.J. 2002, MNRAS, 335, 843

Paczyński, B., & Wiita, P. 1980, A&A, 88, 23

Phinney, E.S. 1989, IAU Symp. 136: The Center of the Galaxy, 543

Portegies Zwart, S. F., et al. 2004, Nature, 428, 724

Price, D.J. & Monaghan, J.J., MNRAS 2007, 374, 1347

Ramirez-Ruiz, E. & Rosswog, S. 2008, arXiv:0808.3847

Reid, I. N. 2005, ARA&A, 43, 247

Rees, M. J. 1988, Nature, 333, 523

Rosswog, S., et al. 2000, A&A, 360, 171

Rosswog, S., Speith, R., & Wynn, G. A. 2004, MNRAS, 351, 1121

Rosswog, S., ApJ 2005, 634, 1202

Rosswog, S. & Price, D.J., MNRAS 2007, 379, 915

Rosswog, S., Ramirez-Ruiz, E., Hix, W. R., & Dan, M. 2008, Computer Physics Communications, 179, 184

Rosswog, S., Ramirez-Ruiz, E., & Hix, W. R. 2008, ApJ, 679, 1385

Rosswog, S. & Price, D., Springer Lecture Notes in Computational Science and Engineering, in press (2008), arXiv0802.0418R

Salaris, M. et al. 1997, ApJ, 486, 413

Springel, V. & Hernquist, L. MNRAS 2002, 333, 649

Straniero, O. and Domínguez, I. and Imbriani, G. & Piersanti, L. 2003, ApJ, 583, 878

Timmes, F. X. & Swesty, F. D. 2000, ApJS, 126, 501

Weidemann, V. 1990, ARA&A, 28, 103

Wilson, J. R., & Mathews, G. J. 2004, ApJ, 610, 368

This manuscript was prepared with the AAS LaTeX macros v5.2.

Table 1: Summary of the performed runs. $M_{\rm wd}$ and $M_{\rm BH}$ are the masses of the white dwarf and the black hole, respectively, β is the ratio of tidal radius and pericentre distance. The type of gravity is indicated by N (Newtonian) or PW (Paczyński-Wiita). Column six states the number of SPH particles used in the simulation, $E_{\rm burn}$ is the energy generated in burning processes. To put this number into context we briefly state the gravitational binding energies (in ergs) of the different white dwarfs: $\log(E_{{\rm bin},0.2M_\odot}) = 49.13$, $\log(E_{{\rm bin},0.6M_\odot}) = 50.12$, $\log(E_{{\rm bin},1.2M_\odot}) = 50.98$. "Fe" labels the mass in iron-group elements, "expl." in the comment column indicates that the produced nuclear energy exceeds the WD gravitational binding energy.

run	$M_{\rm wd}$	$M_{\rm BH}$	β	grav	SPH part.	$\log(E_{\rm burn})$	"Fe" [$M_\odot$]	comments
1	0.2	1000	12	N	4034050	50.46	0.025	expl.
2	0.2	1000	12	PW	4034050	50.44	0.034	expl.
3	0.2	1000	12	PW	200452	50.44		$\Gamma = 5/3$-polytrope
4	0.2	100	5	PW	100027	49.57	$< 10^{-10}$	explore BH influence, expl.
5	0.2	500	5	PW	100027	49.64	$< 10^{-10}$	explore BH influence, expl.
6	0.2	1000	5	PW	100027	49.76	$< 10^{-10}$	explore BH influence, expl.
7	0.2	5000	5	PW	100027	49.93	$< 10^{-10}$	explore BH influence, expl.
8	0.6	500	5	N	502479	50.68	0.18	expl.
9	0.6	500	5	N	502479	50.62	0.13	hot, initial WD
10	0.6	1000	0.9	N	1006446	0.00	0.	no nuclear burning
11	0.6	1000	5	PW	502479	50.43	3×10^{-4}	
12	0.6	10000	1.5	PW	502479	45.07	$< 10^{-10}$	
13	1.2	100	3.5	N	100027	51.01	0.58	expl.
14	1.2	500	2.6	PW	502479	51.16	0.66	expl.
15	1.2	1000	1.5	PW	502479	49.63	0.014	
16	1.2	1000	3.0	N	502479	51.10	0.63	expl.

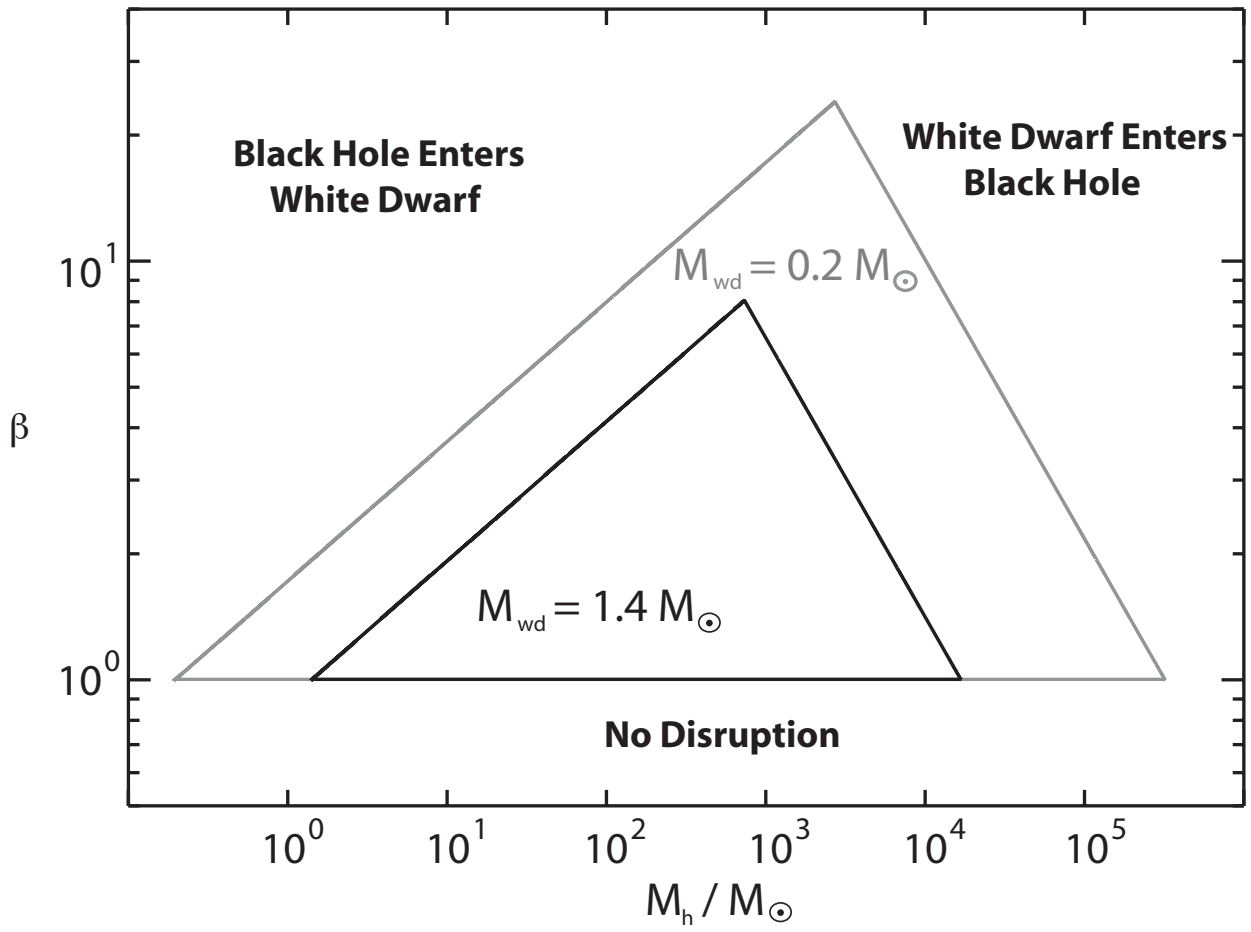

Fig. 1.— This diagrams depicts the relevant domain where the black hole's tidal effect can be disruptive to a white dwarf star. The penetration factor β is plotted as a function of the black hole mass $M_{\rm BH}$. Note that a black hole of $\gg 10^5 M_\odot$ can swallow all white dwarfs without first disrupting them (adapted from Luminet & Pichon 1989).

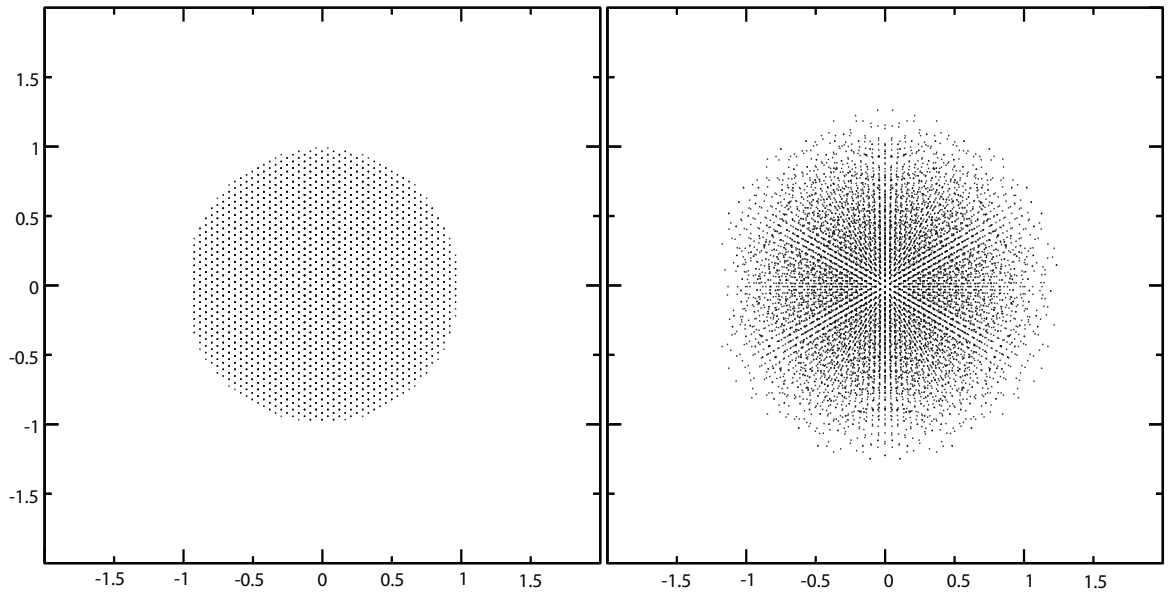

Fig. 2.— Building initial conditions by solving the spherically symmetric Lane-Emden equations for a star of given mass and composition to find a one dimensional density profile. The particles are then distributed inside a unit sphere according to a close-packed prescription. *Left Panel:* Close-packed particle distributions in a unit sphere. This distribution is then mapped into the volume of the star that is to be constructed. *Right Panel:* Particle distribution after mapping onto the density profile of a 0.2 $M_{\odot}$ white dwarf. Shown are the projections of the particle positions onto the xy-plane. This particle distribution is then finlly 'relaxed' into its true numerical equilibrium.

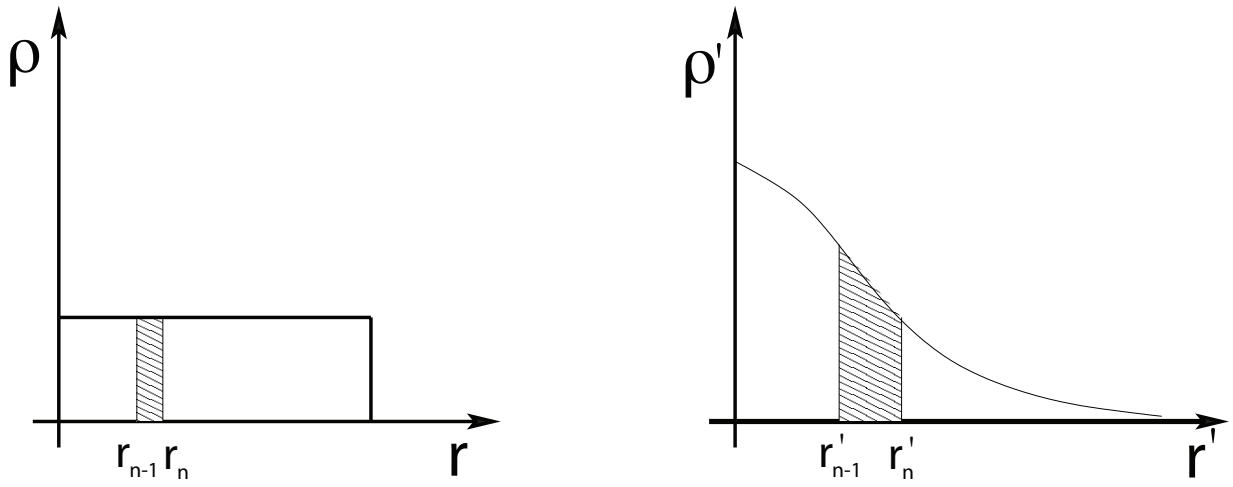

Fig. 3.— Mapping between unit sphere and star. We denote quantities referring to the star (unit sphere) with (un-)primed variables.

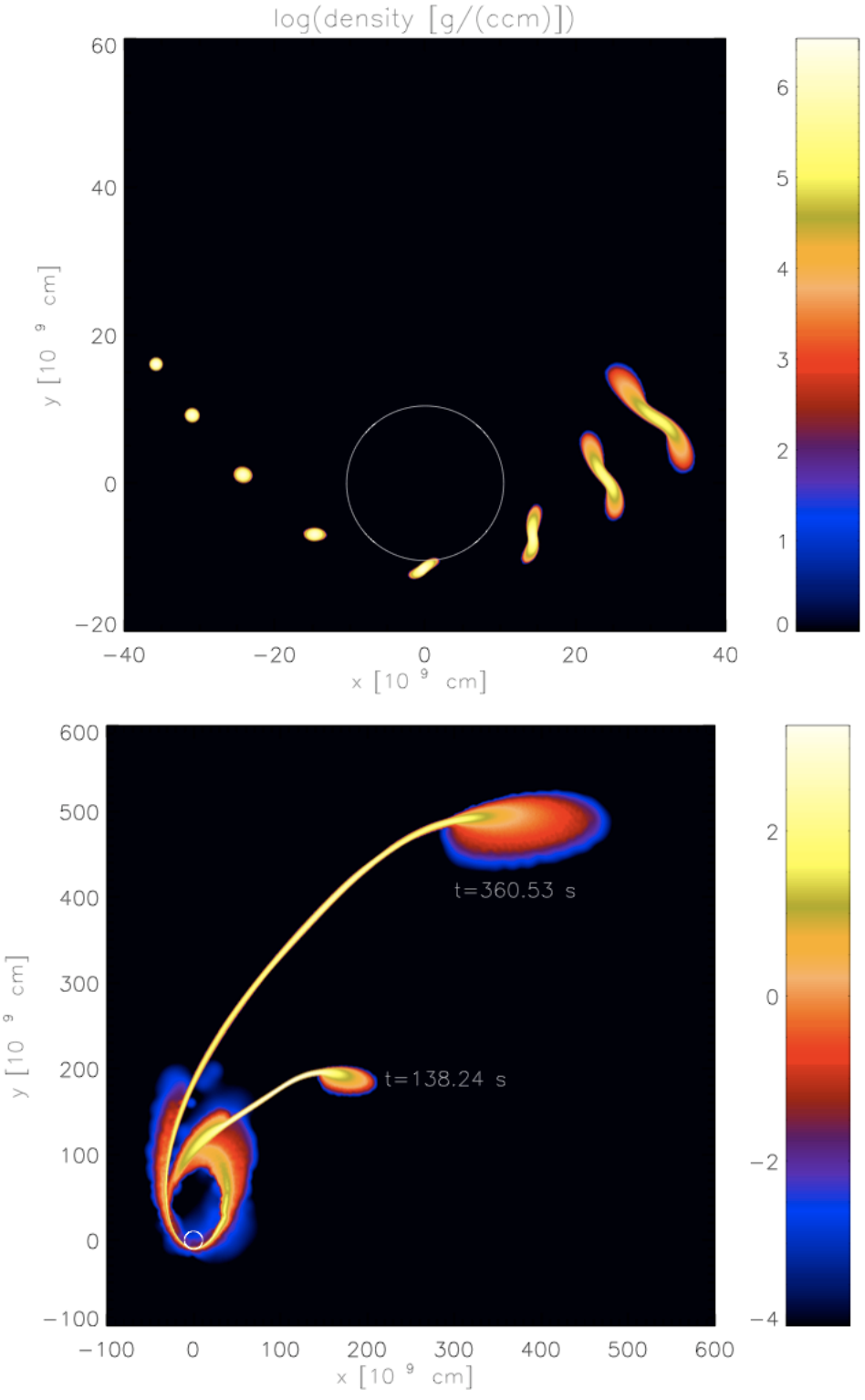

Fig. 4.— Evolution of a 0.6 $M_\odot$ white dwarf passing a 1000 $M_\odot$ black hole with a penetration factor β of only 0.9. The snapshots show t= 0.34, 3.43, 6.86, 10.29, 13.72, 17.15, 20.58 and 24.01 s after the simulation start in the upper, and 138.24 and 380.53 s in the lower panel.

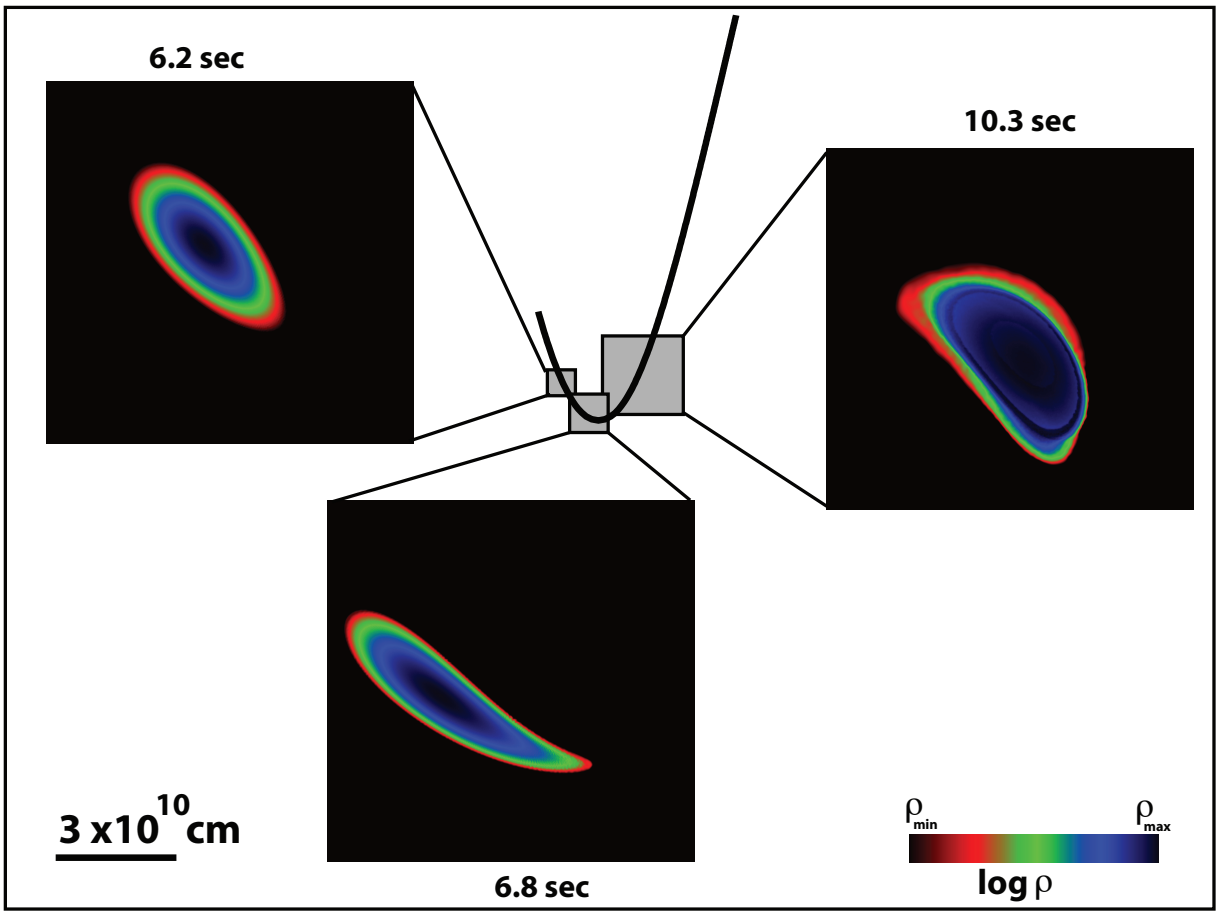

Fig. 5.— A 0.2 $M_\odot$ white dwarf (modeled with more than 4×10^6 SPH particles) approaching a 10^3 $M_\odot$ black hole on a parabolic orbit with pericenter distance $R_{\rm p} = R_\tau/12$ is distorted, spun up during infall and then tidally disrupted. Shown are density cuts at various instants along the orbital (xy-) plane. Color bar gives the amplitude of $\log\rho = [\log\rho_{\rm max}, \log\rho_{\rm min}]$ in cgs units: $[4.0, 5.3]$ for t=6.2 s, $[3.6, 5.4]$ for t=6.8 s, and $[0, 3.4]$ for t=10.3 s.

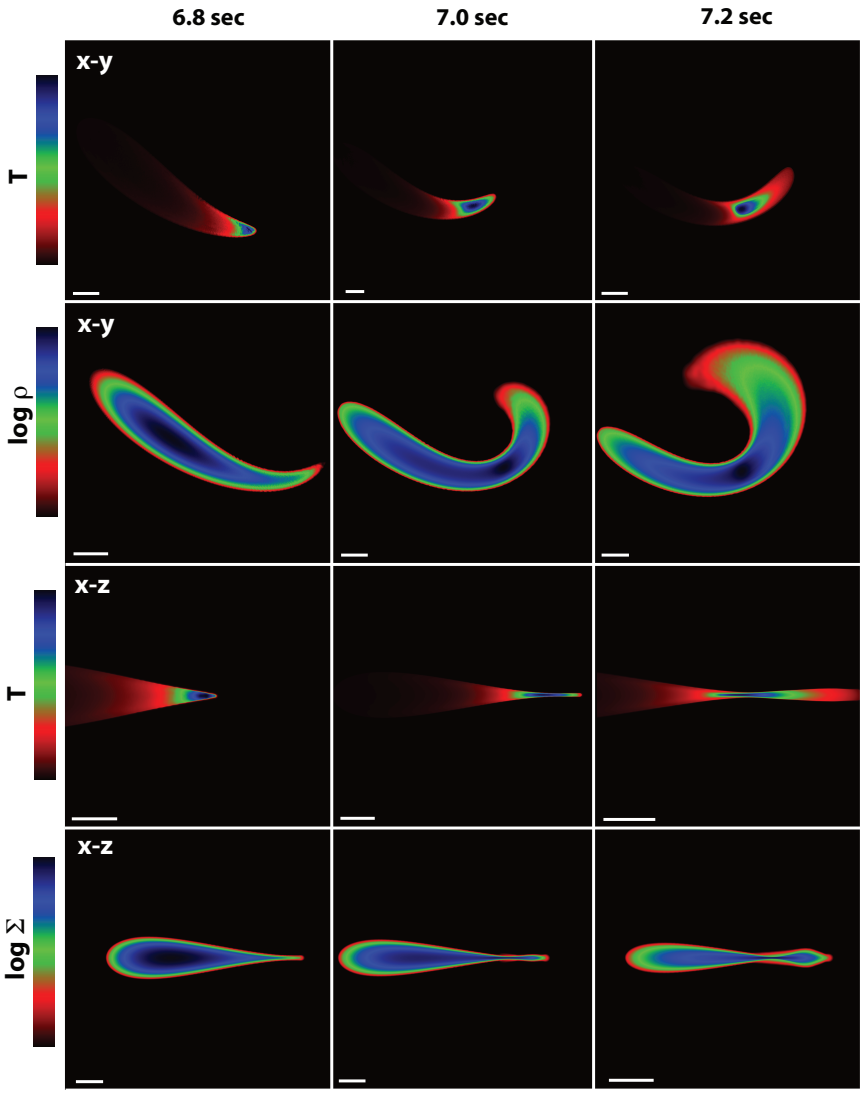

Fig. 6.— Tidal deformation of the white dwarf before and after passage through pericenter, as the star attains its maximum degree of compression (same simulation as referred to in Figure 5). The panels in the upper rows show cuts of temperature (in units of 10^6 K) and density (in cgs units) through the orbital (xy-) plane. Color bar gives the values of $T = [T_{\rm min}, T_{\rm max}]$ ($\log \rho = [\log \rho_{\rm min}, \log \rho_{\rm max}]$): $[0, 330]$ ($[3.6, 5.4]$) for t=6.8 s, $[0, 1280]$ ($[1.0, 6.0]$) for t=7.0 s, and $[0, 3200]$ ($[1.0, 6.0]$) for t=7.2 s. The panels in the lower two rows show the temperature (in units of 10^6 K) and column density (in cgs units) distributions in the xz-pane (averaged along the y-direction). Color bar gives the values of $T = [T_{\rm min}, T_{\rm max}]$ ($\log \Sigma = [\log \Sigma_{\rm min}, \log \Sigma_{\rm max}]$): $[0, 220]$ ($[12.0, 15.7]$) for t=6.8 s, $[0, 720]$ ($[12.0, 16.0]$) for t=7.0 s, and $[0, 1700]$ ($[12.0, 16.5]$) for t=7.2 s. The dimension of the bar scale is 10^9 cm.

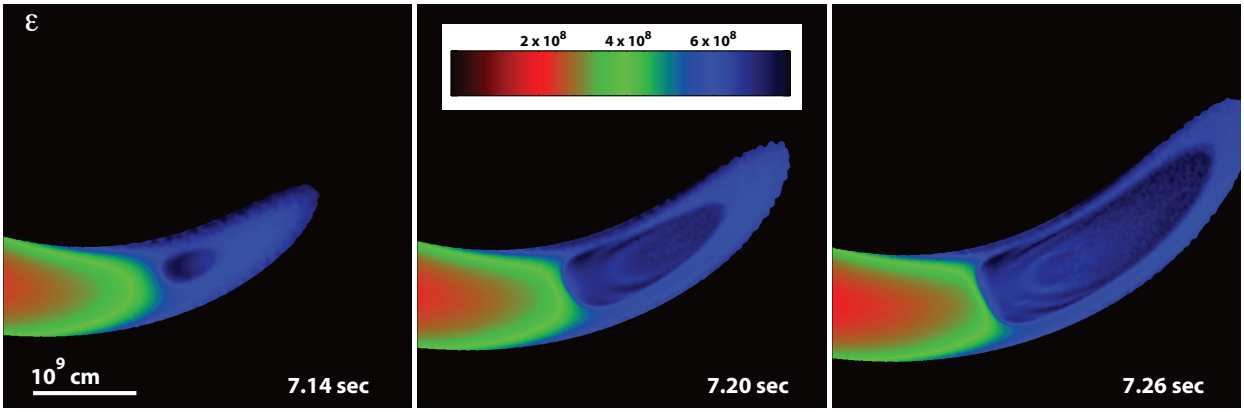

Fig. 7.— Evolution of the entropy ε of the central portion of the disrupted white dwarf just after it attains its maximum degree of compression (same simulation as referred to in Figures 5 and 6). This compression is halted by a shock, raising the matter to a higher adiabat. The panels show entropy (in cgs units) cuts through the orbital (xy-) plane.

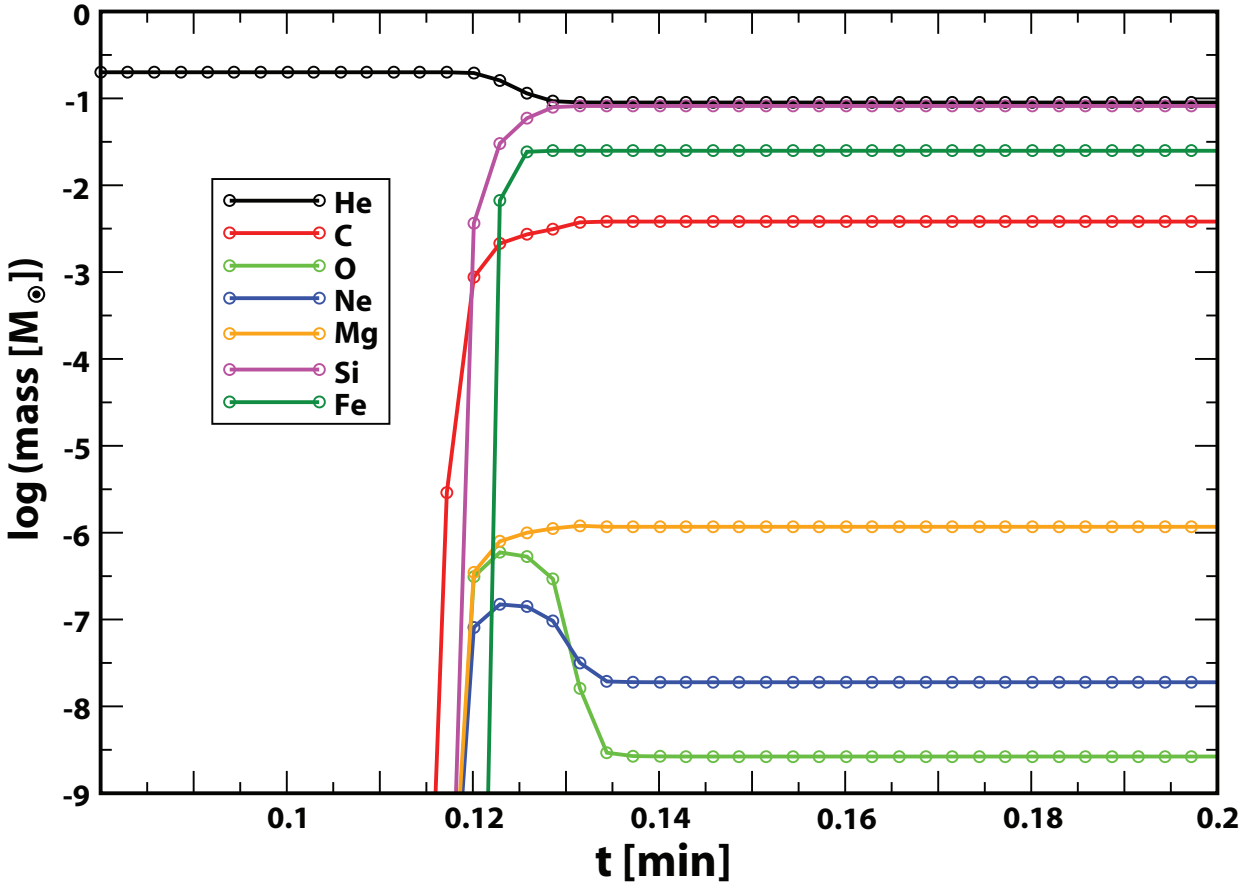

Fig. 8.— Evolution of the abundances during the disruption and ignition of a 0.2 $M_\odot$ white dwarf passing a $10^3 M_\odot$ black hole (same simulation as referred to in Figures 5–7).

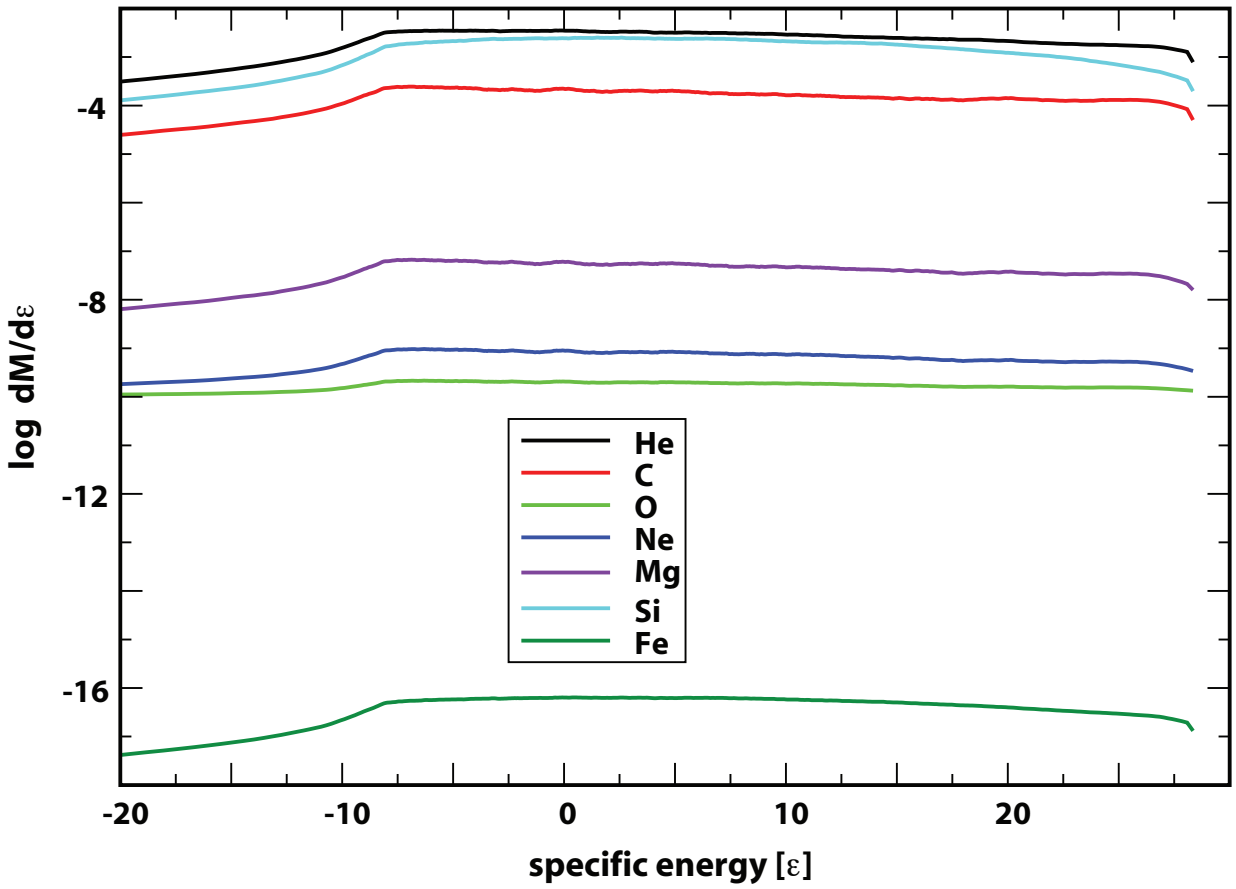

Fig. 9.— Differential mass distributions in specific energy for the 0.2 $M_{\odot}$ white dwarf debris (same simulation as referred to in Figures 5–8).

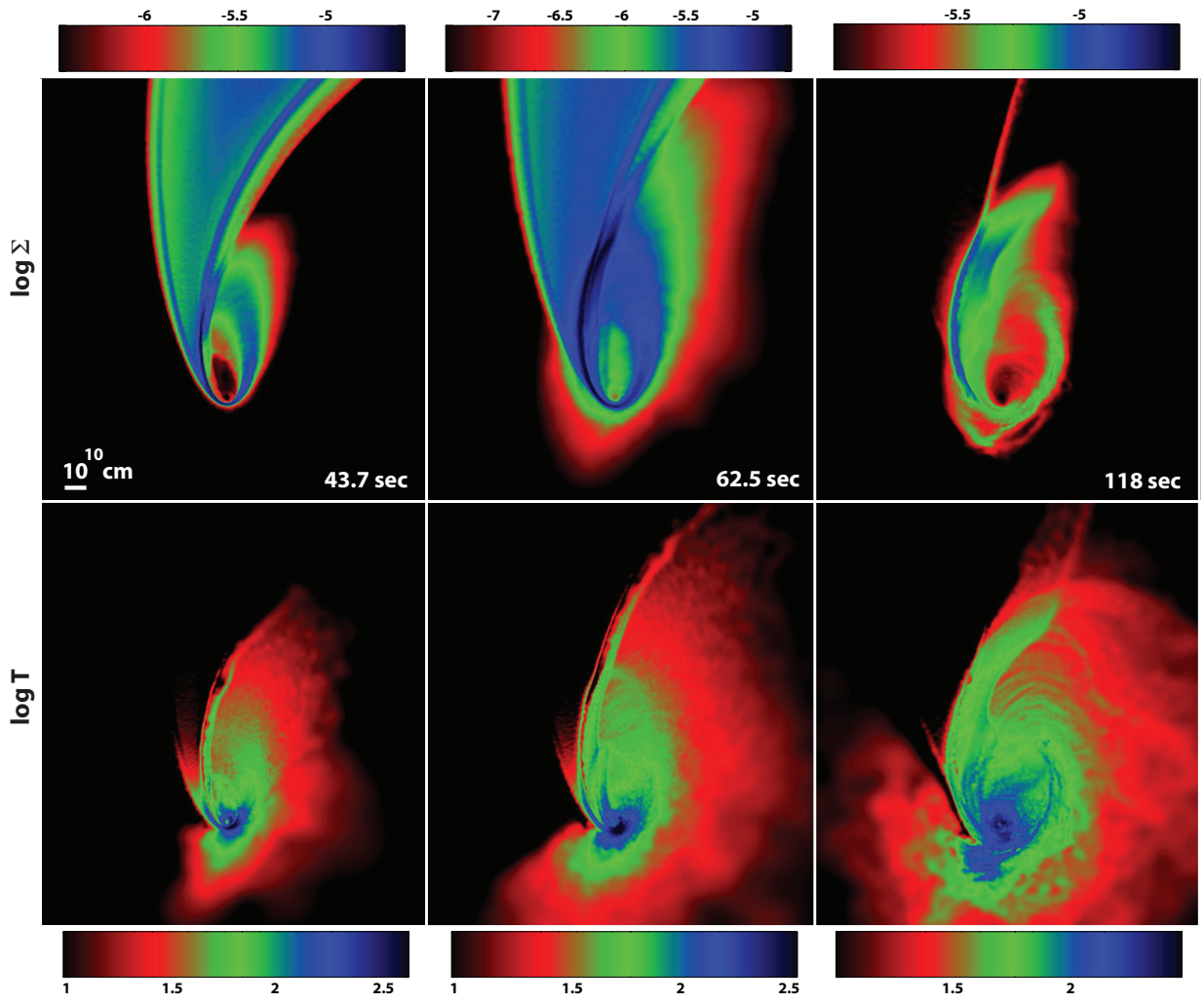

Fig. 10.— Column density (in cgs units) and temperature (in units of 10^6 K) distributions in the orbital plane of the bound debris minutes after disruption. The most tightly bound debris would transverse an elliptical orbit with major axis $\sim 300R_{\rm g}$ before returning to $R \approx R_\tau$ (same simulation as referred to in Figures 5–9).

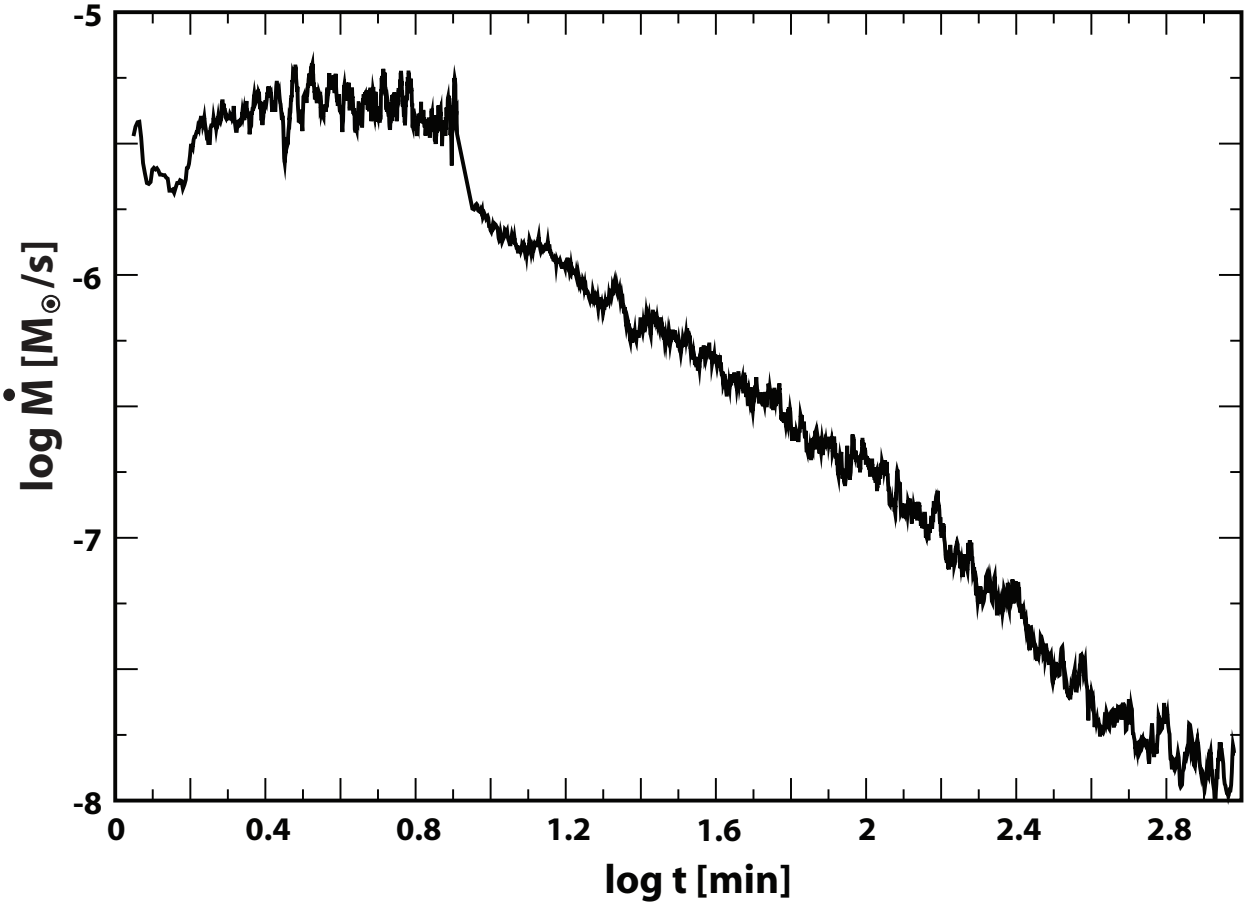

Fig. 11.— The rate at which the 0.2 $M_{\odot}$ white dwarf debris returns to the vicinity of the black hole (same simulation as referred to in Figures 5–10).

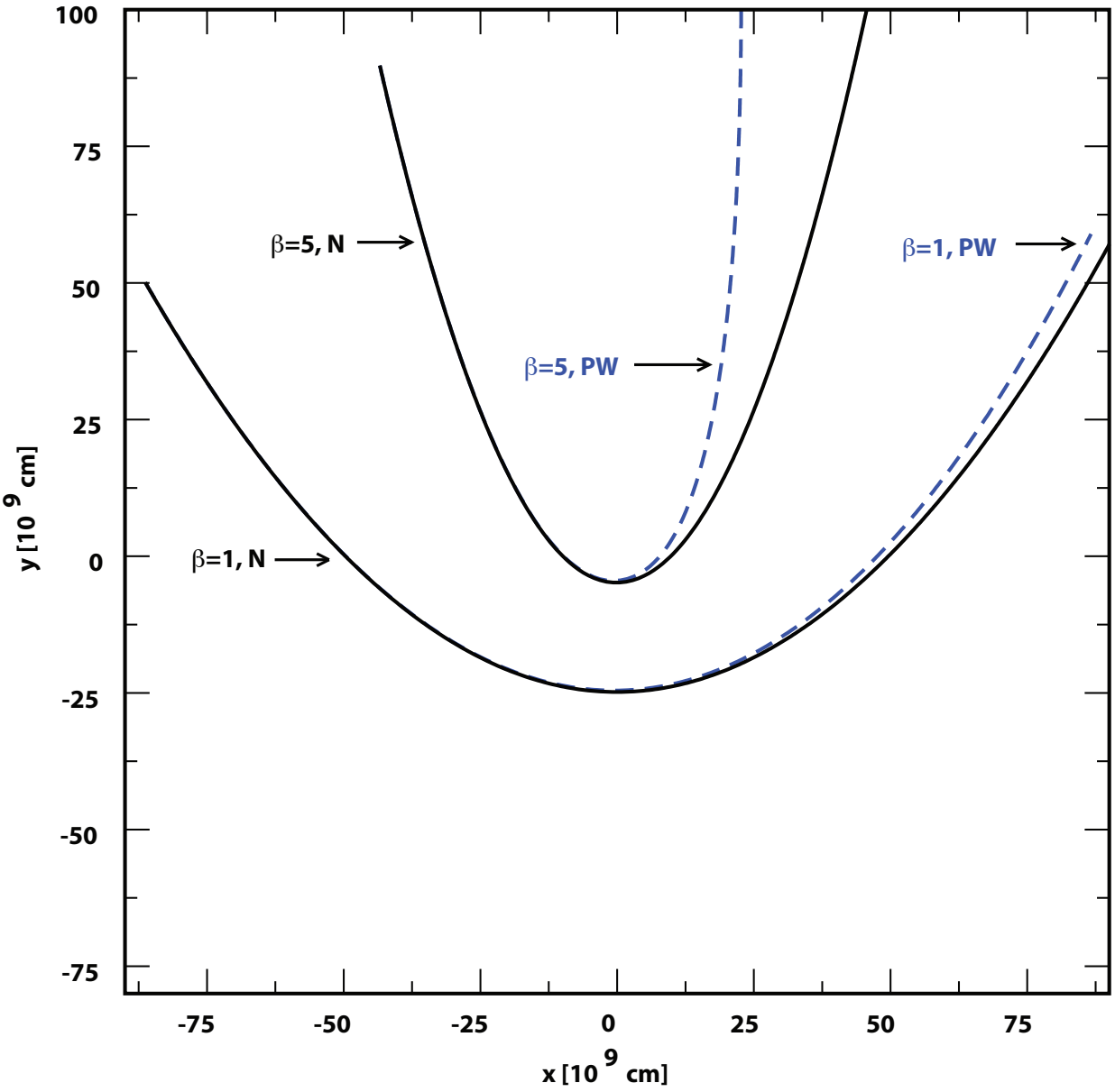

Fig. 12.— The importance of relativistic effects from the central black hole in determining the behavior of white dwarfs passing within the tidal radius. The trajectory of the center of mass of a 0.2 $M_\odot$ white dwarf approaching a 10^3 $M_\odot$ black hole on a parabolic orbit with impact parameter β are shown using Newtonian gravity (N; black) and the pseudo-Newtonian relativistic potential of Paczyński-Wiita (PW, blue). Each time, the star is modeled with more than 10^5 partices.

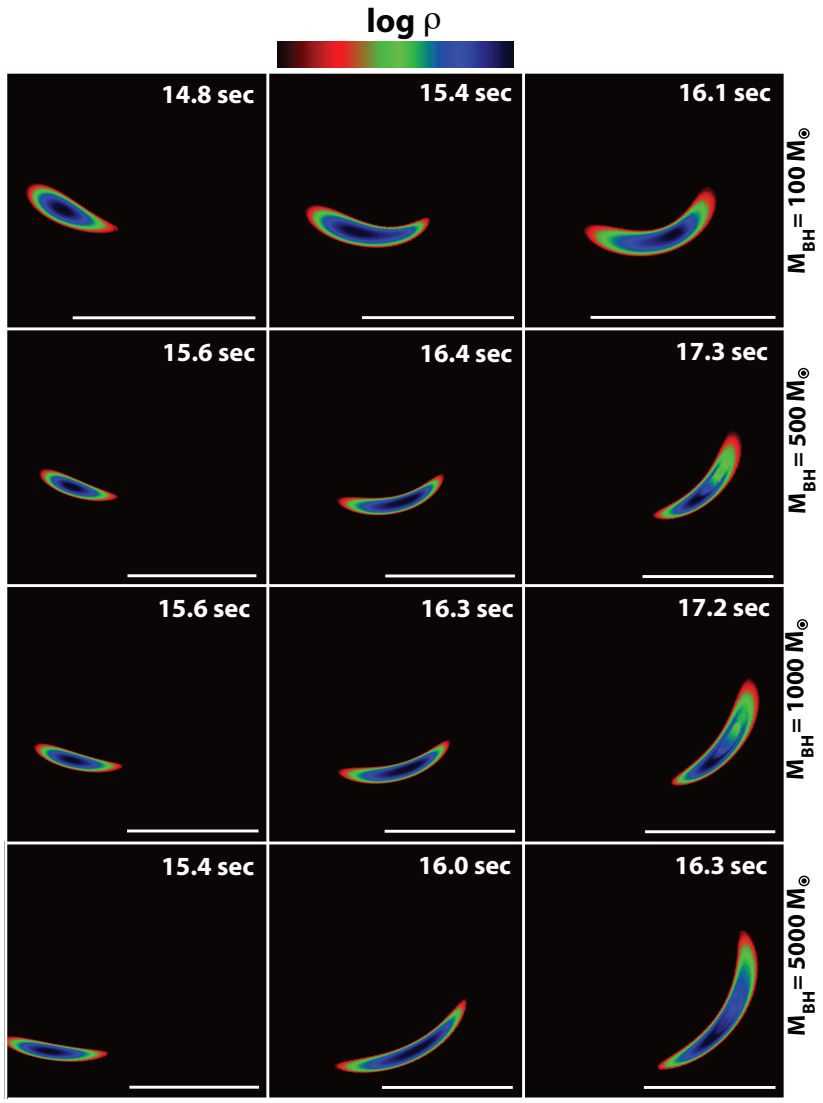

Fig. 13.— A 0.2 $M_\odot$ white dwarf approaching black holes of various masses on a parabolic orbit with $\beta = 5$. The panels in the show density (in cgs units) cuts through the orbital (xy-) plane. Color bar gives the values of $\log \rho = [\log \rho_{\rm min}, \log \rho_{\rm max}]$. For $M_{\rm BH} = 10^2 M_\odot$, $\log \rho = [4.25, 5.3]$ for t= 14.8 s, $[4.0, 5.4]$ for t= 15.4, and $[3.75, 5.8]$ for t= 16.1. For $M_{\rm BH} = 5 \times 10^2 M_\odot$, $\log \rho = [4.15, 5.3]$ for t= 15.6 s, $[3.9, 5.65]$ for t= 16.4, and $[3.75, 5.8]$ for t= 17.3. For $M_{\rm BH} = 10^3 M_\odot$, $\log \rho = [4.1, 5.4]$ for t= 15.6 s, $[3.9, 5.65]$ for t= 16.3, and $[3.4, 5.6]$ for t= 17.2. For $M_{\rm BH} = 5 \times 10^3 M_\odot$, $\log \rho = [4.0, 5.4]$ for t= 15.4 s, $[3.7, 5.75]$ for t= 16.0, and $[3.4, 5.8]$ for t= 16.3.

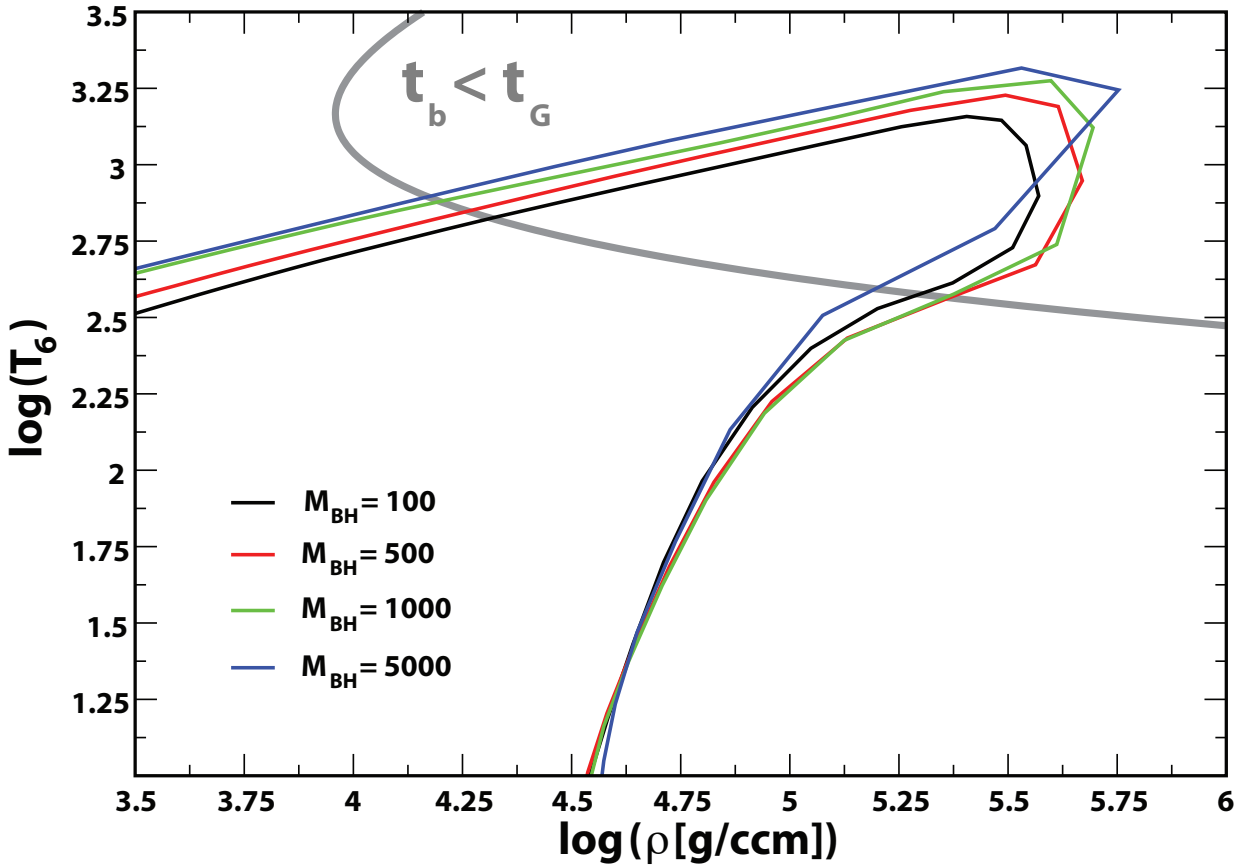

Fig. 14.— The importance of the central black hole's mass in determining the behavior of a 0.2 $M_\odot$ white dwarf passing within $\beta = 5$ (same simulations as referred to in Figure 13). The evolution of the compressed, and tidally disrupted white dwarf in the $\rho - T$ plane. The hottest 10% of the particles are identified and their average temperature (in units of 10^6 K) is plotted as a function of their average density (in cgs units). These trajectories always start cold and dense (right lower corner) and become hot and during the black hole flyby. If the time scale on which the white dwarf can react (dynamical time scale $t_{\rm G}$) is longer than the burning time scale ($t_{\rm b}$, see Eq. (18)), the star cannot expand rapidly enough to quench burning.

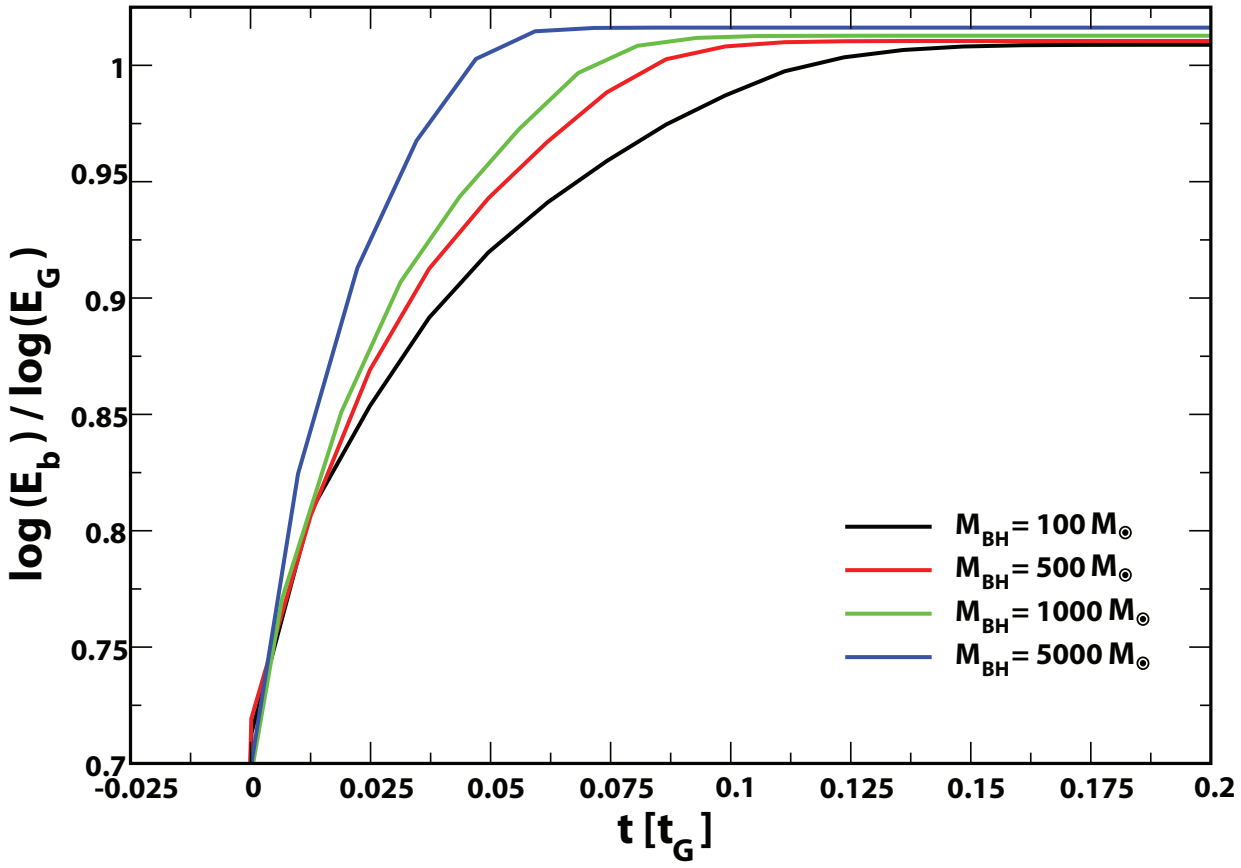

Fig. 15.— Energy generated in nuclear burning (in units of the star's binding energy) as a function of time (same simulations as referred to in Figures 13 and 14). Here time is measured in units of the dynamical timescale ($t_{\rm G}$) of the initial 0.2 $M_{\odot}$ white dwarf. In addition, the time axis has been shifted so that the maximum $E_{\rm b}$ occurs at $t = 0$.

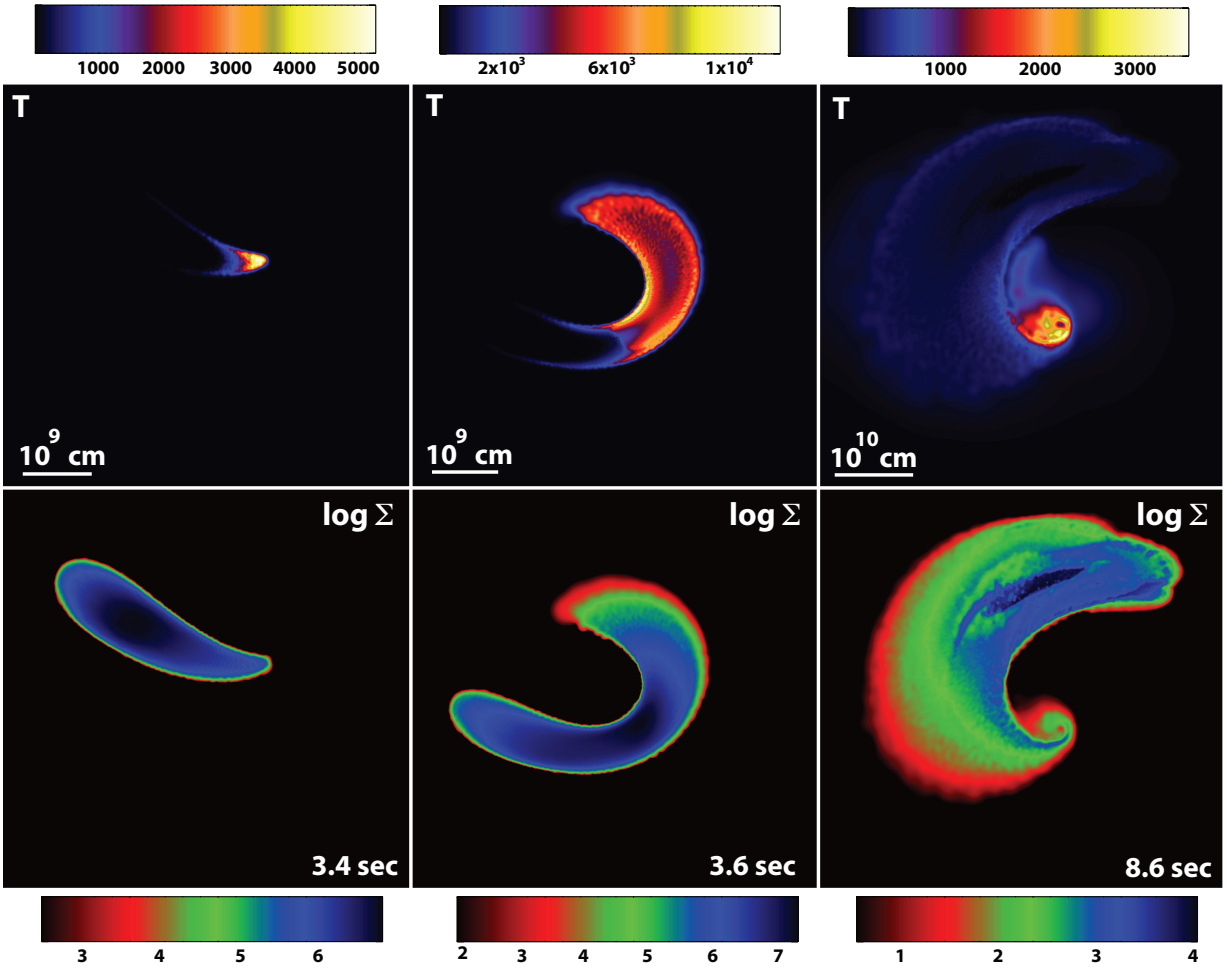

Fig. 16.— A 1.2 $M_\odot$ white dwarf (modeled with more than 5×10^5 SPH particles) approaching a 500 $M_\odot$ black hole on a parabolic orbit with pericenter distance $r_{\rm min} = r_{\rm T}/3.2$. Shown are temperature (in units of 10^6 K) and surface density (in cgs units) cuts at various instants along the orbital (xy-) plane.

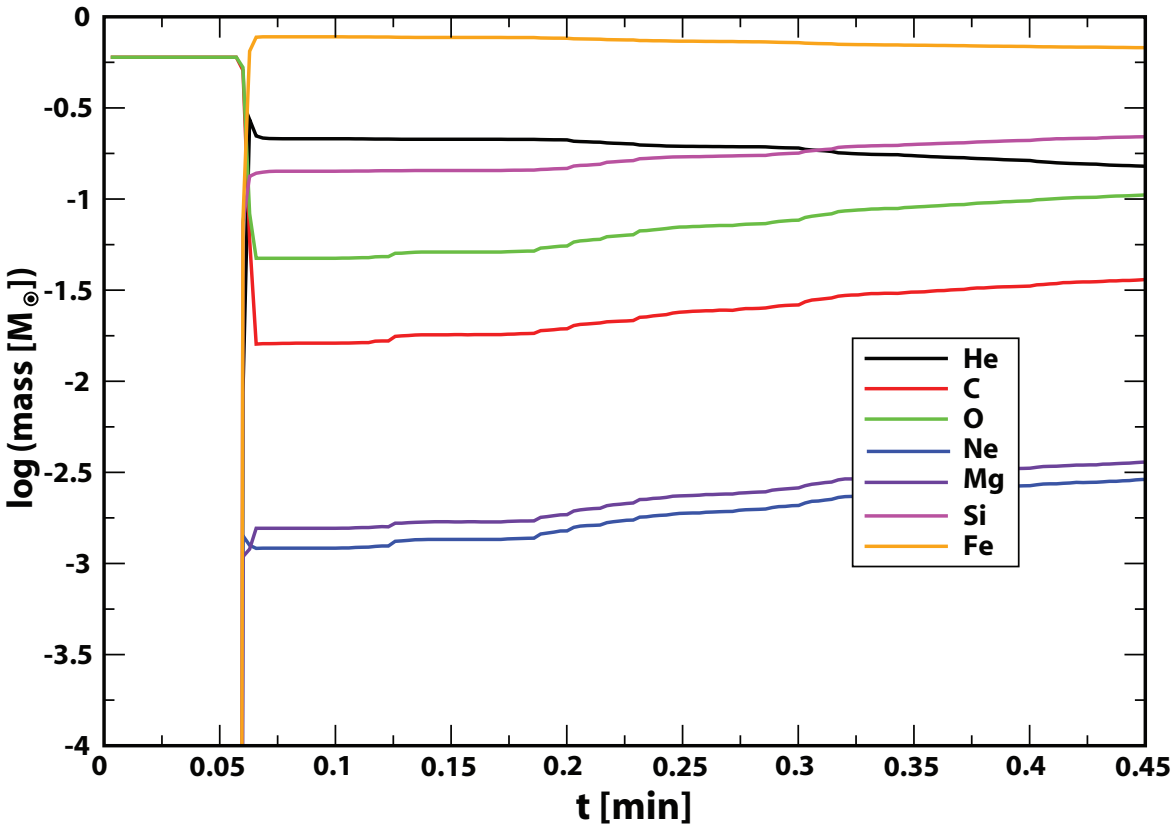

Fig. 17.— Evolution of the abundances during the disruption and ignition of a 1.2 $M_{\odot}$ white dwarf approaching a $500M_{\odot}$ black hole (same simulation as referred to in Figure 16).

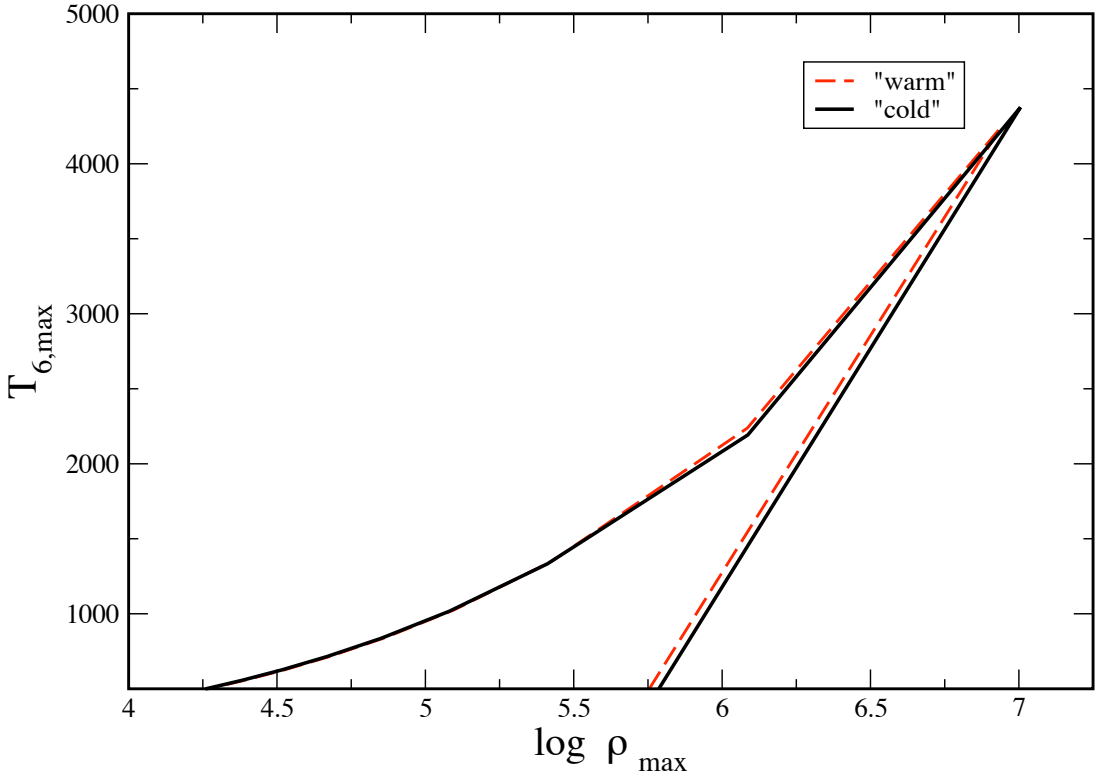

Fig. 18.— Comparison of the average properties of the hottest 10% of the SPH particles for an initially cold and warm star (runs 8 and 9 in Table 1).

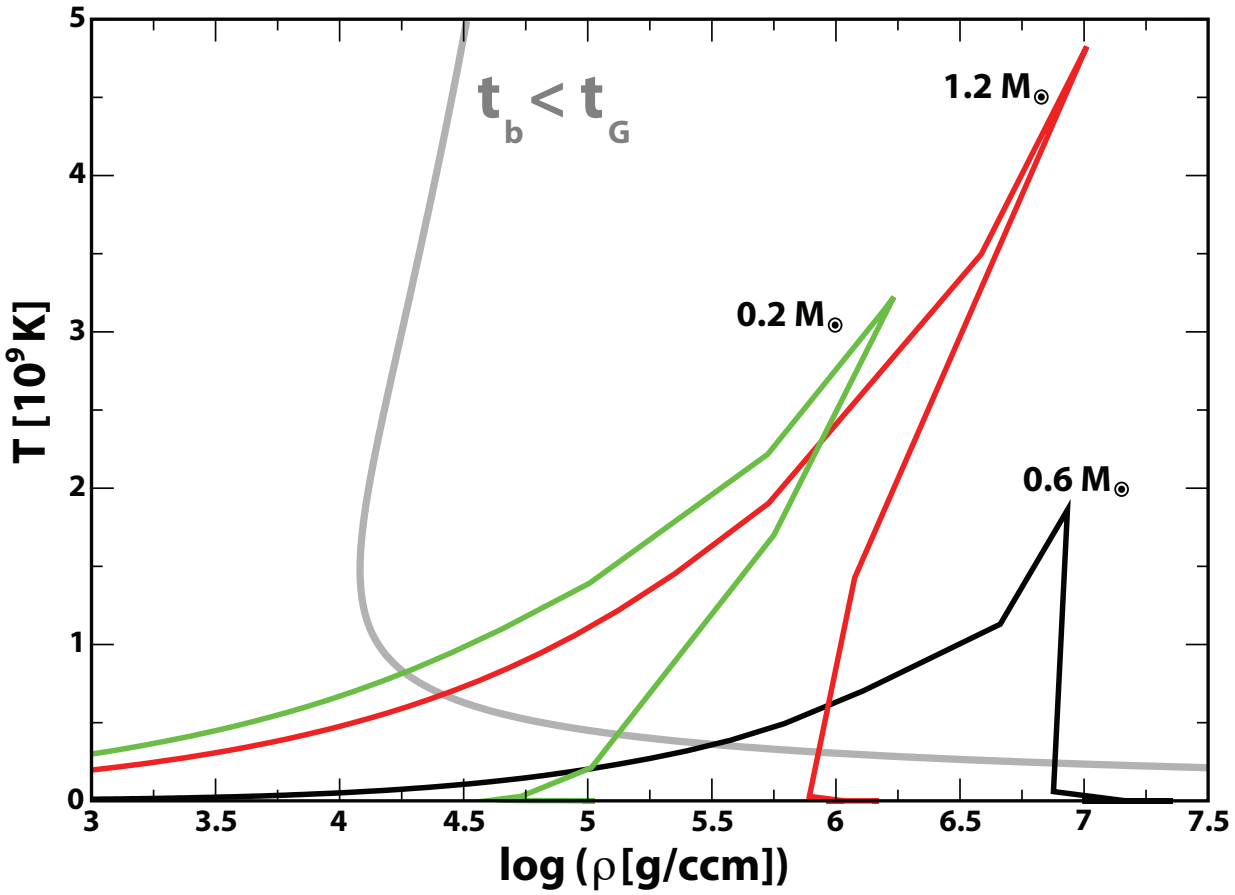

Fig. 19.— The evolution of the compressed, and tidally disrupted white dwarfs of various masses in the $\rho - T$ plane: A 0.2 He $M_\odot$ white dwarf approaching a $10^3 M_\odot$ black hole with $\beta = 12$; a 0.6 C/0 $M_\odot$ white dwarf approaching a $10^4 M_\odot$ black hole with $\beta = 1.5$ and a 1.2 C/0 $M_\odot$ white dwarf approaching a $10^3 M_\odot$ black hole with $\beta = 1.5$. The hottest 10% of the particles are identified and their average temperature (in units of 10^6 K) is plotted as a function of their average density (in cgs units). These trajectories always start cold and dense (right lower corner) and become hot and during the black hole flyby. For the 1.2 $M_\odot$ and 0.6 $M_\odot$ cases, the time scale on which the white dwarf can react is similar to the burning time scale and the star expands rapidly enough to quench explosive energy release.

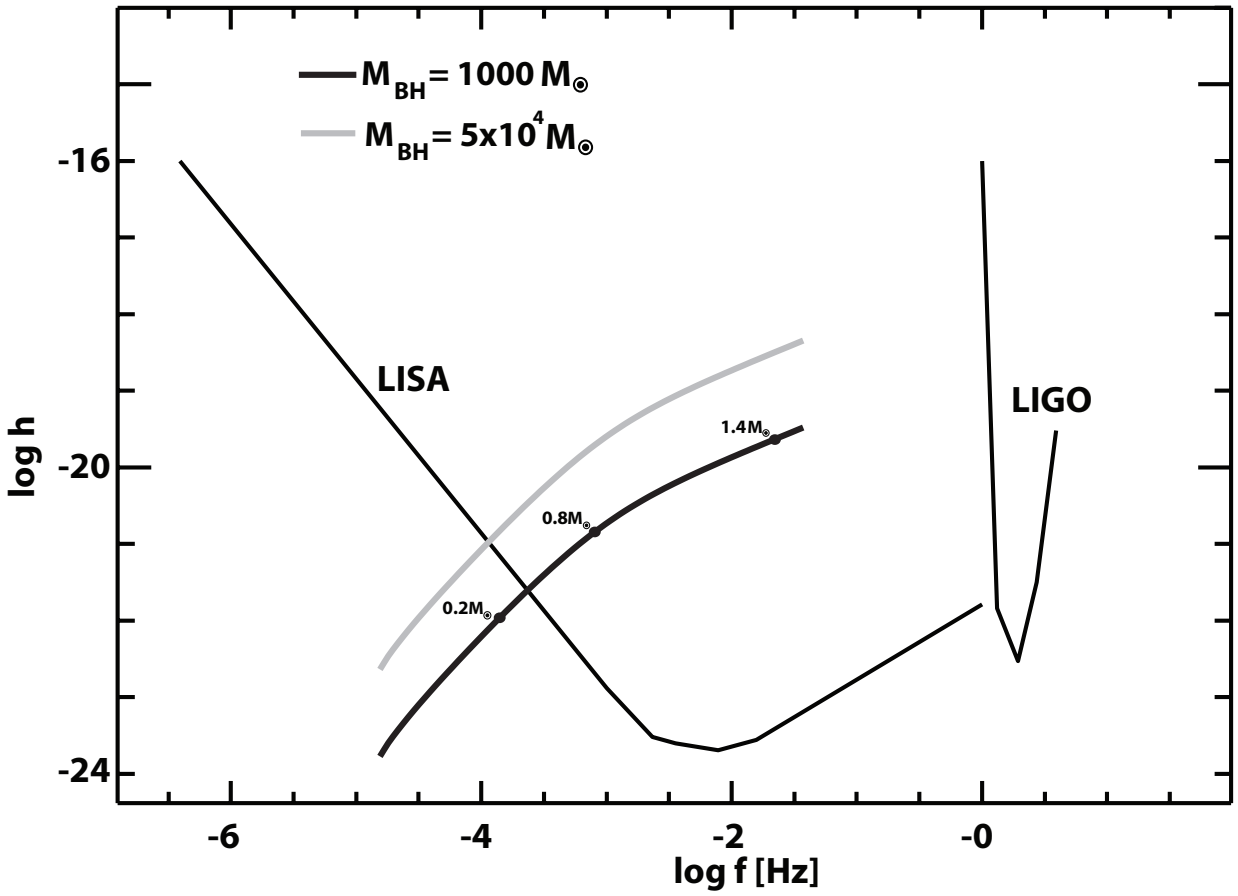

Fig. 20.— Frequency and amplitude of gravitational radiation produced by the disruption of white dwarfs approaching an intermediate mass black hole, assuming $\beta = 1$ and that the cluster hosting the black hole is at $D = 8$kpc.

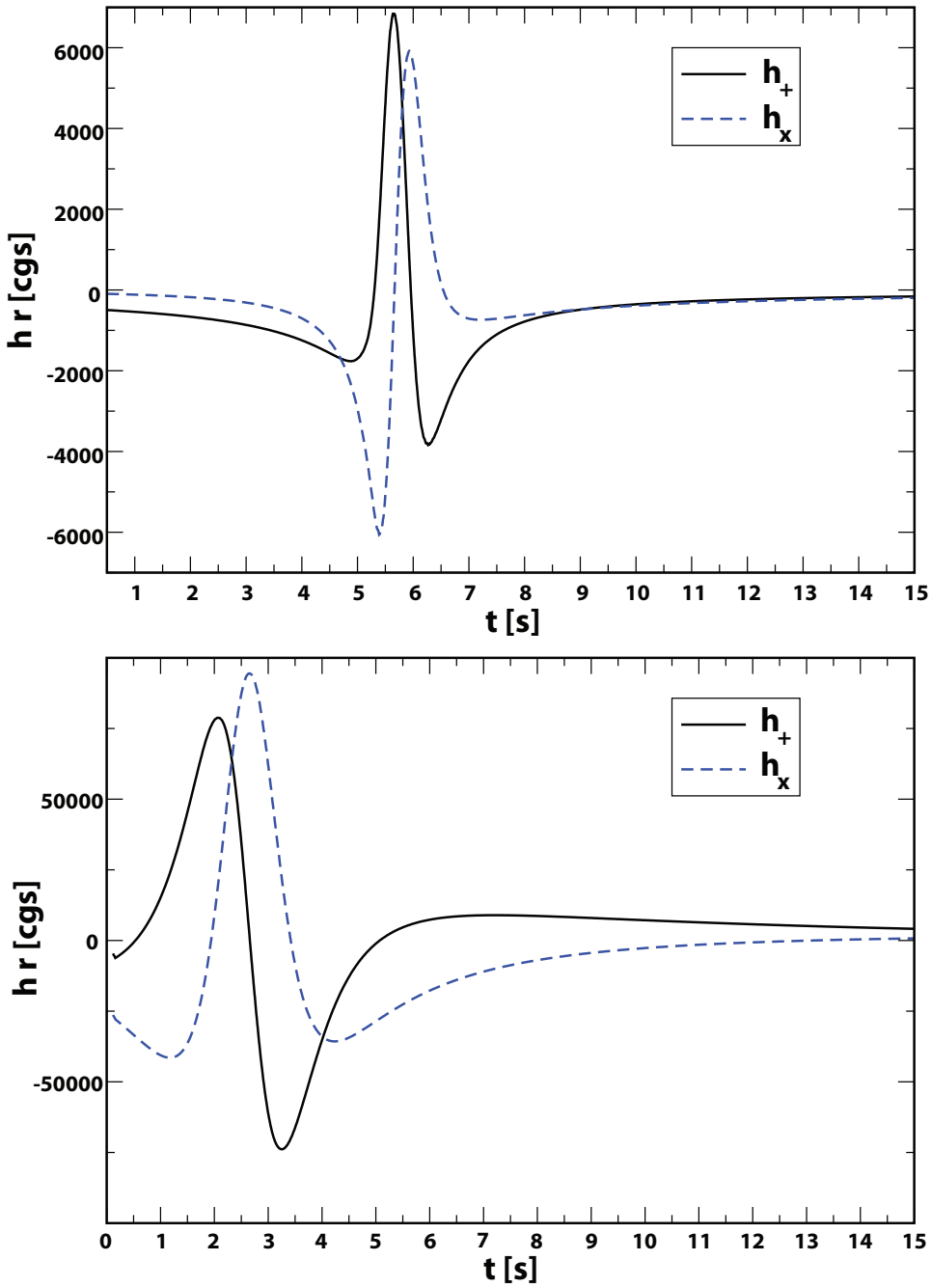

Fig. 21.— Gravitational wave amplitudes. *Top panel:* gravitational radiation produced by the disruption of a 0.2 $M_\odot$ white dwarf approaching a $10^3 M_\odot$ black hole with $\beta = 12$. *Bottom panel:* gravitational radiation produced by the disruption of a 0.6 $M_\odot$ white dwarf approaching a $10^4 M_\odot$ black hole with $\beta = 1.5$.